



**HAL**  
open science

# Transient Nodal Signaling in Left Precursors Coordinates Opposed Asymmetries Shaping the Heart Loop

Audrey Desgrange, Jean-François Le Garrec, Ségolène Bernheim, Tobias Holm Bønnelykke, Sigolène Meilhac

► **To cite this version:**

Audrey Desgrange, Jean-François Le Garrec, Ségolène Bernheim, Tobias Holm Bønnelykke, Sigolène Meilhac. Transient Nodal Signaling in Left Precursors Coordinates Opposed Asymmetries Shaping the Heart Loop. *Developmental Cell*, 2020, 55 (4), pp.413-431.e6. 10.1016/j.devcel.2020.10.008 . hal-03094810

**HAL Id: hal-03094810**

**<https://hal.science/hal-03094810>**

Submitted on 15 Dec 2022

**HAL** is a multi-disciplinary open access archive for the deposit and dissemination of scientific research documents, whether they are published or not. The documents may come from teaching and research institutions in France or abroad, or from public or private research centers.

L'archive ouverte pluridisciplinaire **HAL**, est destinée au dépôt et à la diffusion de documents scientifiques de niveau recherche, publiés ou non, émanant des établissements d'enseignement et de recherche français ou étrangers, des laboratoires publics ou privés.



Distributed under a Creative Commons Attribution - NonCommercial 4.0 International License

## Title

# **Transient Nodal signalling in left precursors coordinates opposed asymmetries shaping the heart loop**

## Authors/Affiliations

Audrey Desgrange<sup>1</sup>, Jean-François Le Garrec<sup>1</sup>, Ségolène Bernheim<sup>1</sup>, Tobias Holm Bønnelykke<sup>1,2</sup> and Sigolène M. Meilhac<sup>1,3\*</sup>

<sup>1</sup> Université de Paris, *Imagine* - Institut Pasteur, Unit of Heart Morphogenesis, INSERM UMR1163, F-75015, Paris, France

<sup>2</sup> Sorbonne Université, Collège Doctoral, 75005 Paris, France

<sup>3</sup> Lead Contact

\* Correspondence to Sigolène Meilhac, [sigolene.meilhac@institutimagine.org](mailto:sigolene.meilhac@institutimagine.org)

**Summary**

The secreted factor Nodal, known as a major left determinant, is associated with severe heart defects. Yet it has been unclear how it regulates asymmetric morphogenesis such as heart looping, which align cardiac chambers to establish the double blood circulation. Here, we report that Nodal is transiently active in precursors of the mouse heart tube poles, before looping. In conditional mutants, we show that Nodal is not required to initiate asymmetric morphogenesis. We provide evidence of a heart-specific random generator of asymmetry that is independent of Nodal. Using 3D quantifications and simulations, we demonstrate that Nodal functions as a bias of this mechanism: it is required to amplify and coordinate opposed left-right asymmetries at the heart tube poles, thus generating a robust helical shape. We identify downstream effectors of Nodal signalling, regulating asymmetries in cell proliferation, differentiation and extra-cellular matrix composition. Our study highlights how Nodal regulates asymmetric organogenesis.

**Keywords** : Nodal signalling, left-right asymmetry, heart morphogenesis, congenital heart defects, 3D imaging

## Introduction

Left-right asymmetric organogenesis is essential for vertebrates. Impairment of left-right patterning leads to human diseases such as the heterotaxy syndrome, affecting the asymmetry or concordance of the positions of visceral organs (Van Praagh, 2006). Heterotaxy is associated with complex congenital heart defects which determine the prognosis of patients (Lin et al., 2014). Asymmetric organogenesis has been theorised by (Brown and Wolpert, 1990) to occur in two sequential steps: (1) a symmetry-breaking event, transforming molecular chirality into a left-right bias, which coordinates laterality throughout the embryo ; (2) organ-specific random generators of asymmetry, which generate asymmetric organ shapes and are modulated by the left-right bias. Studies of the left-right organiser support step (1), whereas random generators of asymmetry in step (2) are still poorly characterised.

How the bilateral symmetry is broken in the early embryo is now well established. This involves a left-right organiser, referred to as the node in the mouse, which forms as a pit of ciliated cells at embryonic day (E)7.5 (see Lee and Anderson, 2008; Shiratori and Hamada, 2006). The motility of cilia generates a leftward fluid flow (Nonaka et al., 1998), which is required between the 1 to 6 somite stages for the asymmetric expression of components of Nodal signalling. *Dand5*, encoding a Nodal antagonist, is the first gene asymmetrically expressed, on the right side of the perinodal region (Kawasumi et al., 2011; Marques et al., 2004). As a result, Nodal, a secreted factor of the TGF $\beta$  family, becomes active only on the left side of the perinodal region, as detected by the phosphorylation of the Smad2 transcription factor (Kawasumi et al., 2011). It stimulates its own asymmetric expression in the left perinodal region and the left lateral plate mesoderm (Brennan et al., 2002; Saijoh et al., 2003). *Nodal* expression is initiated lateral to the node, then propagates anteriorly and posteriorly in the left lateral plate mesoderm by auto-activation (Lowe et al., 1996; Vincent et al., 2004). Nodal also activates its own antagonists *Lefty1/2*, suggestive of a patterning mechanism by reaction-diffusion as shown in the fish blastula (Müller et al., 2012). The negative feedback loop ensures transient expression of *Nodal* in the lateral plate mesoderm, where heart precursors are localised, between the 3 and 6 somite stages. *Nodal* is not expressed within the heart tube (Collignon et al., 1996; Vincent et al., 2004). Deletion of the asymmetric enhancer (ASE) of *Nodal* dramatically reduces left-sided *Nodal* expression and impairs the formation of the heart and lungs (Norris et al., 2002). Similarly, the conditional inactivation of *Nodal* in the mesoderm impairs left-right asymmetry of the heart, lungs, spleen and stomach (Kumar et al., 2008). Nodal is thus a major left determinant, required in the

lateral plate mesoderm for asymmetric organogenesis. The phenotype of *Nodal* mutants is either symmetrical, i.e. right isomerism as seen in the lungs, spleen and atria, or randomly lateralised, as seen in the stomach, gut, heart apex or heart tube (Brennan et al., 2002; Kumar et al., 2008; Lowe et al., 2001; Saijoh et al., 2003). Beyond its asymmetric expression in cell precursors of the lateral plate mesoderm, it has remained unclear by which mechanism Nodal regulates the morphogenesis of visceral organs.

The primordium of the heart is a tube, which grows by addition of precursor cells from the heart field to the arterial (cranial) and venous (caudal) poles (Domínguez et al., 2012; Kelly et al., 2001). The heart becomes asymmetrical during the process of heart looping, which transforms the tubular primordium into a helix. This process, which has been extensively studied in the chick embryo, is crucial to position the cardiac chambers relative to each other and thus establish the double blood circulation (see Desgrange et al., 2018). From 3D (dimensions) reconstructions in the mouse embryo at E8.5, we have previously characterised the spatiotemporal dynamics of heart looping, and established specific staging criteria (Fig. 1A). A model for a heart-specific random generator of asymmetry was proposed (Le Garrec et al., 2017). This is based on buckling, when the heart tube grows between fixed poles, as a mechanism able to generate random deformations. We uncovered sequential and opposed asymmetries at the poles, which can bias the buckling to generate a helix: a rightward rotation of the arterial pole at E8.5f, followed by an asymmetric ingression of heart precursors at the venous pole at E8.5g. Finally, the progressive breakdown of the dorsal mesocardium provides an additional mechanical constraint that reinforces looping, as suggested also by inhibition of matrix metalloproteases in the chick (Linask et al., 2005). On these bases, we have generated a computer model, which can predict the shape of the heart loop, not only its direction, thus providing an original framework to analyse asymmetric heart morphogenesis. However, the molecular mechanisms of the left-right asymmetries at the heart tube poles remain unknown.

*Nodal* (Brennan et al., 2002; Kumar et al., 2008; Lowe et al., 2001; Saijoh et al., 2003), or components of *Nodal* signalling such as the transcription factor *Foxh1*, the co-receptor *Cfc1*, or the protease *Furin* (Both et al., 2004; Roebroek et al., 1998; Yan et al., 1999), have been shown to control the direction of the heart loop. These studies have focused on the binary looping direction, as a readout of the symmetry-breaking event, but have not addressed the specific shape of the heart helix, as a readout of the heart-specific generator of asymmetry. In addition to heart looping, left-right patterning of cardiac precursors is important for the left-right identity of atrial chambers and the morphogenesis of the outflow

tract. Clonal analyses of myocardial cells have shown a differential origin of the pulmonary and aortic trunks from left and right precursors respectively (Lescroart et al., 2010; 2012). In keeping with the spiralling of the great arteries in the mature heart, the outflow tract undergoes a rightward rotation (Bajolle et al., 2006), which follows that of the arterial pole during heart looping (Le Garrec et al., 2017). Regionalisation of the outflow tract prefigures the separation of the great arteries, as marked by *Sema3c* (Théveniau-Ruissy et al., 2008). Outflow tract defects have been associated with *Nodal* mutations in mouse models (Kumar et al., 2008; Lowe et al., 2001; Saijoh et al., 2003) and in patients, including a higher occurrence of pulmonary atresia and transposition of the great arteries (Bouvagnet and de Bellaing, 2016; Mohapatra et al., 2008).

A pending question is the identification of the molecular effectors downstream of Nodal signalling, and how they control asymmetric cell behaviour during organogenesis. Targets of the Nodal pathway have been mainly identified in the context of zebrafish gastrulation (Bennett et al., 2007), ES cell differentiation (Brown et al., 2011) or in cell cultures (Coda et al., 2017; Guzman-Ayala et al., 2009), but not in the context of left-right asymmetric organogenesis. A target gene of Nodal signalling in the left lateral plate mesoderm is the isoform *Pitx2c*, which is expressed asymmetrically in the heart tube, mainly in the inner curvature (Campione et al., 2001; Furtado et al., 2011), and regulates asymmetric cell proliferation and atrial cell identity (Galli et al., 2008). However, contrary to Nodal, *Pitx2* or its isoform *Pitx2c* are not required for the proper direction of heart looping (Liu et al., 2002; Lu et al., 1999), highlighting the existence of other Nodal target genes during this process.

Here, we address the specific role of Nodal for mouse heart looping with a high spatiotemporal resolution. We mapped the cardiac precursor cells expressing *Nodal* and determined the time window of Nodal activity. We generated conditional *Nodal* mutants, using *Hoxb1<sup>Cre</sup>* to target the mesoderm. We combined quantifications of the heart shape in 3D and computer simulations to assess how Nodal controls the heart-specific generator of asymmetry. Our results show that the generator of asymmetry is independent of Nodal, and that Nodal is required to amplify and bias pre-existing asymmetries at the tube poles. We show that *Pitx2c* is not required for mediating the biasing signal of Nodal. By transcriptomic analyses, we identify other targets of Nodal, involved in the regulation of asymmetric cell behaviour at the heart tube poles. Overall, Nodal is essential for the robust rightward helical shape of the heart. This has functional impact for the blood circulation, given that heart looping underlies the alignment of cardiac chambers.

## Results

### ***Nodal* is expressed in myocardial precursors contributing to a quarter of the heart poles**

Since *Nodal* is transiently expressed in the left lateral plate mesoderm and not within the heart tube, we investigated whether *Nodal*-expressing cells are genuine heart precursors. We took advantage of the *Nodal-ASE-lacZ* transgenic line, in which the  $\beta$ -galactosidase is produced under the control of the asymmetric enhancer of *Nodal*. The known perdurance of *lacZ* mRNA and/or  $\beta$ -galactosidase (Echelard et al., 1994) provides a pulse-chase readout of *Nodal* expression in the left lateral plate mesoderm. By 3D imaging of stained embryos at progressive stages of heart looping (Fig. 1A),  $\beta$ -galactosidase positive cells were found not only in the left second heart field, but also in the inner curvature of the heart tube poles : in the left sinus venosus, the myocardium of the dorsal left atrium, of the superior atrio-ventricular canal and of the left outflow tract (Fig. 1B-G, Movie S1). A sharp boundary was observed within the right ventricle and at the entrance of the left ventricle, such that the two ventricles at E9.5 were largely devoid of  $\beta$ -galactosidase staining (Fig. 1H). In the outflow tract, the domain positive for *Sema3c*, a marker of the pulmonary trunk (Théveniau-Ruissy et al., 2008), is broader and includes that of *Nodal-ASE-lacZ* (Fig. 1I-J). No staining was observed in the endocardium (Movie S1). After segmentation of the heart tube myocardium, we measured that a fraction of  $17\% \pm 5$  (n=16) is colonised by  $\beta$ -galactosidase positive cells, at all stages between E8.5e and E9.5 (Fig. 1K). If we consider only the heart regions colonised by  $\beta$ -galactosidase positive cells, i.e. discarding the ventricles, the fraction increases to  $26\% \pm 4$  (n=4 at E8.5j and E9.5). Thus we show that left cardiac precursors, which contribute to the ventricles, barely express *Nodal*, whereas left cardiac precursors expressing *Nodal* contribute to a quarter of the cells in the heart tube poles.

### ***Nodal* is transiently active before heart looping, at E8.5c-e**

*Nodal* expression in the lateral plate mesoderm has been previously reported at 3-6 somite stages (Vincent et al., 2004). However, we found that somitogenesis is not synchronised with heart morphogenesis (Kaufman and Navaratnam, 1981; Le Garrec et al., 2017), so we re-analysed *Nodal* expression within the context of heart looping stages. By RT-qPCR of the cardiac region, we found expression of *Nodal* at E8.5c-d (Fig. 2A), which is compatible with the 3-6 somite window. We then assessed the time-window when *Nodal* is active. First we analysed the expression of its target *Lefty2*, which we found expressed at

E8.5c-e, peaking one stage after Nodal (Fig. 2A). Because a mouse litter at E8.5 contains embryos within a range of different looping stages, we used drug treatment in embryo cultures to interfere with Nodal signaling at a specific stage. The SB505124 drug was shown previously to efficiently abrogate Alk signaling (DaCosta Byfield et al., 2004; Hagos and Dougan, 2007). This includes Nodal/activin receptors (Alk4/7), as well as Tgf $\beta$ 1 receptors (Alk5) that have not been reported to play a role in left-right patterning. When applied to embryos at E8.5c over 8 hours, i.e. until E8.5e, SB505124 repressed the expression of the Nodal-specific target genes *Pitx2* and *Lefty2*, whereas it only decreased it upon treatment at E8.5d and had no effect at E8.5e, compared to treatment with the adjuvant (Fig. 2B-E). Exposure over a shorter period of 4 hours, i.e. until E8.5d, partially reduced *Pitx2* expression. Taken together, these observations indicate a transient time window of Nodal signaling, between E8.5c and E8.5e, thus before heart looping.

### ***Nodal* inactivation in the mesoderm leads to four classes of looping defects**

To study in more detail looping anomalies, we generated *Nodal* conditional mutants, using *Hoxb1*<sup>Cre/+</sup> as a driver that is expressed from the onset of gastrulation in the mesoderm (Forlani et al., 2003), overlapping with *Nodal* asymmetric expression. This provides a model of mesoderm-specific *Nodal* inactivation, different from previous lines (Figure S1). We first collected mutants at birth and found a heterotaxy phenotype, including lung, colon and heart defects (Table 1), but no anomaly in most abdominal organs (intestine, spleen, stomach, liver) as reported in other types of *Nodal* mutant lines (Brennan et al., 2002; Kumar et al., 2008; Lowe et al., 2001 ; Saijoh et al., 2003). Then, we collected embryos at E9.5, when heart looping is complete in wild-type embryos, and analysed the heart phenotype of *Nodal* mutants. In a collection of 56 mutants, we observed 4 classes of anomalies (Fig. 3A), with an equal frequency (Fig. 3B). The classes are defined by the position of the ventricles: inversely lateralised (class 1), both on the right side (class 2), both on the left side (class 3) or normally lateralised (class 4). To confirm the identity of the ventricles, and more generally assess whether heart segments were correctly patterned, we performed a double *in situ* hybridization (ISH), using *Wnt11* as a marker of the outflow tract (Zhou et al., 2007) and *Bmp2* as a marker of the atrio-ventricular canal (Ma et al., 2005) and ventral left atrium. In addition to the sulcus separating the ventricles, this was enough to identify all cardiac segments in a single labelling experiment (Fig. 3C). Staining of *Nodal* mutants indicated normal patterning of the heart tube and confirmed the localisation of the right and left ventricles in the different classes of mutants. To further assess whether mutant phenotypes represent a continuum or discrete



classes, we performed a principal component analysis of the shape of the tube axis, which was extracted as a set of 33 parameters from 3D images by HREM (High Resolution Episcopic Microscopy) (Movie S2). The independent clustering of each class of mutants rules out the hypothesis of a phenotypic continuum (Fig. 3D-E). We conclude that *Nodal* inactivation in the lateral plate mesoderm impairs the positioning of the embryonic ventricles, leading to four possible configurations, with equal frequency. The full penetrance of heart defects at birth such as complete atrioventricular septal defect and malposition of the great arteries (Table 1) indicate that even the milder looping phenotype of Class 4 mutants leads to congenital heart defects.

### ***Nodal* inactivation in the mesoderm randomises heart looping direction**

*Nodal* inactivation was previously reported to randomise the direction of heart looping (Brennan et al., 2002; Kumar et al., 2008; Lowe et al., 2001). However, the method used to assess the loop direction was not defined. Since the looped heart tube has a helical shape, we propose to define the direction of heart looping as the orientation of the tube axis helix, seen cranially at E9.5 (as schematised in Fig. 4B). 3D reconstructions of the heart loop were colour coded for cardiac segments (Fig. 4A, Movie S2-S6) ; the 3D shape of the tube axis was extracted and averaged for at least 5 embryos (Fig. 4B). This shows that heart looping is rightward in class 2 and 4 *Nodal* mutants, as in control littermates, whereas it is leftward in class 1 and 3 mutants. Given the equal frequency of the mutant classes, we conclude that the direction of heart looping is indeed randomised, when *Nodal* is inactivated in the mesoderm. However, the description of the loop direction is not sufficient to characterise heart defects, since mutant classes 2 and 4 or classes 1 and 3 have distinct shapes.

### **Existence of a random generator of asymmetry independent of *Nodal***

Within the framework of the model of heart looping that we have proposed previously (Le Garrec et al., 2017), we analysed whether the associated parameters are affected. Heart looping depends on the buckling of the heart tube, growing between fixed poles. In any class of *Nodal*<sup>flx/null</sup>; *Hoxb1*<sup>Cre/+</sup> mutants, we found no significant difference in growth compared to control littermates (Fig. S2A-F). The distance between the mutant heart poles did not significantly differ from controls (Fig. S2G). Finally, the breakdown of the dorsal mesocardium, which modulates the degree of buckling, occurred normally in the mutant

samples (Fig. S2H). Thus, *Nodal* inactivation affects neither the growth nor the buckling of the heart tube.

In contrast to *Foxh1* mutants, in which ventral loops with no obvious left-right asymmetry were observed (Both et al., 2004), *Nodal* mutant hearts still have an asymmetric shape, though abnormal. We quantified the degree of heart looping in *Nodal* mutants, as evidenced by the progressive repositioning of the right ventricle, which, in control embryos, is cranial at E8.5e and right-sided at E8.5j relative to the left ventricle (Le Garrec et al., 2017). This measure provides a quantitative definition of the discrete classes of mutant hearts, taking into account that the angle is mirror imaged in classes 1 and 3 (Fig. 4C). In none of the mutants has this orientation remained cranio-caudal, indicating an asymmetric deformation of the tube. However, the repositioning of the right ventricle was significantly reduced in *Nodal* mutant classes 1, 2 and 3. These observations point to the persistence of some degree of heart looping in *Nodal* mutants, supporting the idea that a heart-specific random generator of asymmetry remains functional in the absence of *Nodal*.

#### ***Nodal* inactivation affects left-right asymmetries at the heart tube poles**

Our previous computer simulations have shown that the buckling is biased by sequential and opposed left-right asymmetries at the arterial and venous poles. These are important to correctly shape the helix of the heart loop (Le Garrec et al., 2017). One manifestation of these asymmetries is the leftward displacement of the venous pole from E8.5g. This was absent or inverted in 3/5 *Nodal* mutants at E8.5h, when mutant classes cannot be determined (Fig. S3D). At E9.5, the leftward displacement which is accentuated in control embryos, was significantly reduced in class 2, 4 *Nodal* mutants and abrogated (midline location) in class 1, 3 mutants (Fig. 4D). At the arterial pole, we observed anomalies in the curvature of the outflow tract at E9.5. From a cranial view, the outflow tract was significantly straighter in class 1, 3, 4 *Nodal* mutants compared to controls (Fig. 4B, E), whereas in a lateral view, it was straighter in class 1, 2, 3 mutants (Fig. 4F, S3A-B). Earlier at E8.5f, we detected a reduced rotation of the arterial pole in 9 mutants analysed, and 5 cases of reversed direction (Fig. S3C).

When analysing the expression patterns of *Wnt11* and *Bmp2* in 3D, we noticed that they are regionalised in wild-type heart tube poles at E9.5, and that this is not detectable in brightfield images. *Wnt11*, which is a known target of *Pitx2* (Zhou et al., 2007), was found asymmetrically expressed on the left side of the outflow tract at E9.5 (Fig. 4G-H), in a similar domain to *Nodal-ASE-lacZ* (Fig. 1F). *Bmp2* was detected in the left, but not right, ventral

atrium (Fig. 4I). This provides molecular markers of the left-right identities of the heart poles, where sequential and opposed asymmetries are important to shape the heart loop. In *Nodal* mutants, *Bmp2* expression was found correctly left-sided in classes 2 and 4, which loop rightward. In reverse, it was abnormal in classes 1 and 3, which loop leftward (Fig. 4I). However, we observed distinct abnormal patterning of *Bmp2* in the atria : bilateral, partially penetrant, in class 1 mutants, and midline, fully penetrant, in class 3 mutants. Bilateral staining is reminiscent of atrial isomerism, as also detected at birth by the anatomy of atrial appendages (Table 1), whereas midline staining may reflect the position of the atrioventricular canal which fails to be displaced laterally in class 3 mutants (Fig. 4B, D). At the arterial pole of *Nodal* mutants, *Wnt11* expression was also correctly left-sided in classes 2 and 4, whereas it was incorrectly localised to the superior outflow tract in classes 1 and 3, with a partial penetrance in class 1 (Fig. 4G-H). This staining may reflect an abnormal rotation of the outflow tract, as also detected at birth by the malposition of the great arteries (Table 1). Our observations thus indicate that the left-right patterning of the heart poles correlates with the direction of the heart loop (abnormal in classes 1, 3), but *Wnt11/Bmp2* markers are not enough to predict a unique mutant class.

Taken together, our 3D analyses show that *Nodal* is required for the proper shape of the outflow tract, for the correct position of the venous pole and the right ventricle. In class 1 and 3 *Nodal* mutants, leftward looping is associated with more severe anomalies and defective regionalisation of the arterial and venous poles.

### ***Nodal* is required to amplify and coordinate left-right asymmetries**

To understand the mechanism leading to the 4 classes of shapes generated in the absence of *Nodal*, we used our computer model of heart looping (Le Garrec et al., 2017). Based on our observations in *Nodal* mutants, we reasoned that the parameters of buckling itself were normal, whereas the left-right asymmetries at the poles were changed. Randomising the laterality of two parameters (asymmetry at the arterial and venous poles) would be sufficient to generate 4 classes of shapes. However, we also noticed that the shape of control embryos was not observed in mutants. Class 4 mutants are closest to the control phenotype, yet significantly deviate from it (Fig. 4D-E, 5A, C), indicative of incomplete heart looping. In reverse, we also noticed that the leftward loops are not mirror images of the wild-type heart (Fig. 4A, 5B-C), again indicative of incomplete heart looping. Given the reduced asymmetries observed at the poles (Fig. 4D, S3C-D), we thus postulated that they not only had a variable laterality but also a reduced intensity. We simulated a 50% reduction of

intensity, which is within the range of our observations. Computer simulations testing these hypotheses were sufficient to reproduce the 4 classes of mutant shapes, as defined by the position of the ventricles (Fig. 5D compared to 3A). To further validate the simulations, we predicted the orientation of the right ventricle-left ventricle axis in all classes of shapes and observed a remarkable correlation with the biological values (Fig. 5E). The model, including both a randomised laterality and a reduction of asymmetries at the poles, is thus able to recapitulate *Nodal* mutant shapes. Our work demonstrates that *Nodal* is required to amplify and coordinate opposed left-right asymmetries at the poles of the heart tube, thus generating a robust helical shape.

### **Nodal modulates cell proliferation, differentiation and extra-cellular matrix composition**

To understand how *Nodal* could modulate left-right asymmetries at a molecular level, we first analysed its main target, the transcription factor *Pitx2*. We quantified by RT-qPCR that *Pitx2c* is expressed as early as *Nodal* but maintained after E8.5e (Fig. S4A-B). We then analysed mutant embryos, in which the asymmetric enhancer of *Pitx2* is deleted (*Pitx2<sup>ΔASE/ΔASE</sup>*), or the asymmetrically expressed isoform *Pitx2c* inactivated. We detected mild malformations of the heart loop at E9.5 : abnormal patterning of the atria in *Pitx2<sup>ΔASE/ΔASE</sup>* hearts (*Bmp2* in Fig. S4D), which is one aspect of *Nodal* mutants, and malposition of the atrioventricular canal in *Pitx2<sup>ΔASE/ΔASE</sup>* and *Pitx2c<sup>null/null</sup>* mutants (orange arrowheads Fig. S4D-E), which was not observed in *Nodal* mutants. ISH with a probe detecting the three isoforms of *Pitx2*, and RT-qPCR of *Pitx2* isoforms suggest compensation by the *Pitx2a/b* isoforms in the absence of *Pitx2c* (Fig. S4B-C). We then looked at *Pitx2* mutants, in which all three isoforms are inactivated. *Pitx2abc<sup>tm1Sac/tm1Sac</sup>* mutants displayed mild malpositions of the atrioventricular canal (Fig. S4F). 6/12 *Pitx2abc<sup>tm1Jfm/tm1Jfm</sup>* mutants as well as all *Pitx2abc<sup>tm1Sac/tm1Sac</sup>* mutants resemble the mild phenotype of *Pitx2c<sup>null/null</sup>* mutants. 3/12 *Pitx2abc<sup>tm1Jfm/tm1Jfm</sup>* mutants had more severe looping anomalies, as judged by the more cranial position of the right ventricle and the more medial position of the left ventricle, whereas the most severe mutants (3/12) were very similar to class 2 *Nodal* mutants (Fig. S4F compared to Fig. 3A). The leftward displacement of the venous pole was significantly decreased in *Pitx2abc<sup>tm1Jfm/tm1Jfm</sup>* mutants only (Fig. S4G). Thus, *Pitx2* mutants do not phenocopy the full spectrum of heart looping defects in *Nodal* mutants.

To identify other targets of *Nodal*, we used a transcriptomic approach. The heart region (Fig. 6A) was isolated at E8.5e-f, just after *Nodal* extinction (Fig. 2A) and just before

the morphological changes of heart looping. We compared the transcriptome in control and mutant samples. We first validated the dissection and genotype of samples, based on specific markers (Fig. S5A-B). Then, we analysed the GO terms of 481 differentially expressed genes (Table S1, Fig. S5C), showing cell cycle, collagen, chromatin and muscle terms as significantly enriched gene sets. The cell cycle genes *Ccnd2*, *Ccne1*, *Cdc25a*, *Cdc6*, *Cdt1*, *Mcm3/5/10*, *Pcna* were significantly up-regulated in *Nodal* mutants, whereas the cell cycle exit gene *Cdkn1b* was significantly down-regulated (Fig. 6B). To confirm an effect on cell proliferation, we labelled embryos with the mitotic marker phosphorylated histone H3 at different stages of heart looping (Fig. 6C). Since *Nodal* is expressed in the left heart field, we quantified mitotic cells as a ratio between the right and left heart fields. In control embryos, we observed asymmetric proliferation, with significantly more mitotic cells on the right side from E8.5f onwards (Fig. 6D). In contrast, in *Nodal* mutants, no significant asymmetry was observed at E8.5e-i. Thus, molecular and cellular analyses support a role for *Nodal* in controlling the asymmetric proliferation of heart precursors. Differentially expressed genes also include genes involved in cardiomyocyte differentiation, such as *Ttn*, *Tnnt1* and *Vsnll* (Fig. 6E), which are significantly down-regulated in *Nodal* mutants. More generally, in a list of 112 cardiomyocyte differentiation genes (Table S2), the vast majority is slightly down-regulated (Fig. 6E-F). With a statistical bootstrap approach, we conclude that there is a collective significant effect of *Nodal* inactivation on cardiomyocyte differentiation. As a validation, we imaged in 3D the expression pattern of *Tnnt1* and *Vsnll*, encoding a subunit of the slow skeletal troponin and a calcium binding protein respectively (Fig. 6G-H). Expression was detected at the arterial (*Tnnt1*) and venous poles (*Tnnt1*, *Vsnll*). *Tnnt1* was regionalised similarly to *Nodal-ASE-lacZ* (see Fig. 1F) in the left outflow tract and left atrium. Expression of *Tnnt1* was decreased in all *Nodal* mutant classes, and bilateralised in the atria of classes 1-2. Expression of *Vsnll* was decreased at the venous pole (atria and proepicardium) of class 1, 2 and 3 mutants.

Other GO terms characterising genes differentially expressed in controls and *Nodal* mutants relate to collagen and the extra-cellular matrix (Fig. S5C). Several genes encoding extra-cellular matrix proteins, such as *Col1a1/2*, *Col3a1*, *Col5a1/2*, *Col9a3*, *Reln*, *Tnc*, the extra-cellular matrix receptor *Itga2b*, or the matrix metalloproteinase *Mmp9*, were significantly down-regulated in *Nodal* mutants (Fig. 7A). This was validated by 3D imaging of expression patterns. *Tnc* expression, which was detected in the heart precursors and arterial pole (Fig. 7B), as previously reported (Stennard et al., 2005), was reduced in the arterial pole of *Nodal* mutants. We found higher expression of *Mmp9* (Fig. 7C-D) and *Col5a2* (Fig. 7E-F) on the left in control embryos. Expression of *Mmp9* in the outflow tract overlaps with that of

*Pitx2*, indicative of Nodal signaling domain (Fig. 7G). These asymmetries were lost in *Nodal* mutants (Fig. 7C-E).

To gain insights into genes directly regulated by Nodal signaling we performed bioinformatics analyses of the presence of asymmetric enhancers (ASE) in the vicinity of differentially expressed genes, corresponding to a pair of FoxH1 binding sites, as shown previously in the bona fide Nodal direct target genes *Nodal*, *Pitx2* and *Lefty2* (Saijoh et al., 1999; Shiratori et al., 2001). 40% of the genes differentially expressed in *Nodal* mutants, including extra-cellular matrix genes (*Tnc*, *Col5a1/2*, *Col3a1*, *Colla2*, *Itga2b*, *Reln*, ...), and 50% of the cardiomyocyte differentiation genes, such as *Vsnl1*, *Gata4*, *Ttn*, *Mef2c*, *Tbx5*, *Actc1* and *Cacna1d* contained an ASE signature, which is a significant enrichment compared to the total gene list (chi<sup>2</sup> test p=0.036 n=481, 16954 ; p=0.0007 n=112, 16954) (Table S3). All together these results indicate that Nodal signaling controls, in part directly, the asymmetric expression of genes involved in cardiomyocyte differentiation and extracellular matrix composition, whereas it controls indirectly, potentially via *Pitx2*, genes involved in cell proliferation.

Thus, our molecular analyses identify effectors of Nodal signalling, further supporting its role in amplifying left-right asymmetries at the poles of the heart tube.

## Discussion

We have mapped in 3D the asymmetric contribution of *Nodal* expressing precursor cells to the heart tube poles and determined the time-window of Nodal signalling, just before heart looping. Our quantitative analyses in conditional mutants further demonstrate that Nodal does not initiate asymmetric morphogenesis, but rather functions as a biasing signal, to coordinate and amplify opposed left-right asymmetries at the heart tube poles, and thus generate a robust helical shape. We have identified genes downstream of Nodal, which are involved in regulating asymmetries in cell proliferation, differentiation or in the composition of the extra-cellular matrix.

Nodal signalling has been initially identified as the first pathway restricted to the left side of the embryo (Collignon et al., 1996; Levin et al., 1995; Lowe et al., 1996). Nodal is not only required in the node (Brennan et al., 2002), but also in the lateral plate mesoderm (Kumar et al., 2008; Saijoh et al., 2003). Our conditional mutant line indicates a requirement of Nodal in the lateral plate mesoderm for the asymmetric morphogenesis of the heart, lungs and colon, but not for that of the spleen, stomach and gut affected in other *Nodal* mutants (Brennan et al., 2002; Kumar et al., 2008; Lowe et al., 1996; Norris et al., 2002; Saijoh et al., 2003). Using 3D reconstructions and more resolute staging criteria, we now provide a higher spatio-temporal resolution of Nodal signaling in myocardial precursor cells, before heart looping. *Pitx2*, a known target of Nodal, was shown to be dispensable for the proper direction of heart looping (Ammirabile et al., 2012; Liu et al., 2002; Lu et al., 1999), thus ruling out a role for mediating the biasing function of Nodal. Our mutant analysis indicates that the ASE enhancer of *Pitx2* is required for the atrial situs, but not for heart looping. Although *Pitx2c* was previously reported as the only asymmetric isoform (Kitamura et al., 1999), we now provide evidence that *Pitx2a/b* isoforms are also expressed in the lateral plate mesoderm and are redundant with *Pitx2c* to modulate heart looping. Upon inactivation of the three *Pitx2* isoforms, anomalies of ventricle position had been reported (Kitamura et al., 1999; Lin et al., 1999; Martin et al., 2010), which we find, in the most severe cases, similar to one class of *Nodal* mutants. *Pitx2* mutants also display specific anomalies, not detected in *Nodal* mutants, such as malposition of the atrioventricular canal, in agreement with previous reports (Kitamura et al., 1999; Lu et al., 1999). Thus, *Pitx2* mediates aspects of Nodal signaling and has also independent roles. Our transcriptomic analysis identifies targets of Nodal signalling, modulating the proliferation, differentiation and extra-cellular matrix composition of cardiac cells, providing a mechanism for how Nodal may generate or amplify molecular left-right asymmetries. Several of these targets (*Tnnt1*, *Vsnl1*, *Col5a2*, *Mmp9* and

*Tnc*) are expressed asymmetrically in the heart tube poles or heart field, in agreement with the contribution of *Nodal* expressing cells. Our transcriptomic data highlight downregulation in *Nodal* mutants of many genes involved in myocardial differentiation, including some previously identified in the context of left-right asymmetry, such as *Acta1* (Noël et al., 2013) or *Hcn4* (Pai et al., 2017), whereas *Myh10* expression (Linask et al., 2003) was unchanged. Detection of an ASE enhancer suggests direct regulation by Nodal signaling of half of our gene list, which will have to be confirmed with biochemical approaches. Previous targets of Nodal signalling had been identified in ES cells or during fish gastrulation and mesendoderm specification (Bennett et al., 2007; Brown et al., 2011; Coda et al., 2017; Guzman-Ayala et al., 2009). We have detected little overlap with our gene list (Nodal pathway components, *Cyp26a1*), in keeping with distinct roles of Nodal in distinct tissues and at distinct stages. A common theme is a role of Nodal in cell differentiation, and potentially in cell proliferation and re-arrangements, relevant also to Nodal re-expression during cancer progression and metastasis (see Quail et al., 2013).

The phenotype of asymmetry can be decomposed into several components: the initiation of the asymmetry, the fold difference between the left and right, and the laterality of the difference, i.e. whether a left determinant is localized on the anatomical right or left side. We show that Nodal is not required to initiate asymmetric heart looping. In the absence of *Nodal*, heart looping is not randomized in the sense that specific shapes are generated, rather than a continuum of random shapes. The observation of 4 classes of heart loop shapes with an equal frequency supports the model that independent left-right asymmetries at the two heart poles determine the loop shape. It is the laterality of these asymmetries which is randomised in *Nodal* mutants, but not the process of asymmetry *per se*. Such a biasing role for Nodal has also been reported for the stomach (Kumar et al., 2008; Saijoh et al., 2003), or for the migration of the parapineal nucleus in the fish diencephalon (Concha et al., 2000). In other instances, Nodal is required to initiate asymmetry and its absence leads to symmetrical phenotypes or isomerism. This is the case for atrial identity, the formation of the mouse lungs and spleen (Brennan et al., 2002; Kumar et al., 2008; Lowe et al., 2001; Saijoh et al., 2003), or for the expression of *cxcr4b*, an early marker of the left habenular nucleus in the fish diencephalon (Roussigne et al., 2009). Our quantitative analyses of shape further show that *Nodal* mutant hearts are distinct from the control shape, and from a mirror image. This demonstrates a previously uncharacterised role for Nodal in amplifying left-right asymmetries. Our transcriptomic analysis provides molecular candidates for mediating this amplification. The fact that the reversal of asymmetries does not generate a perfect mirror image of organs may explain why situs inversus totalis (incidence 3/100,000) is not always



asymptomatic, but can be associated with anomalies in the heart, spleen and intestinal rotation (Lin et al., 2014).

Our study supports the two-step model of asymmetric organogenesis proposed by Brown and Wolpert (1990) and provides a demonstration of the concept of an organ-specific random generator of asymmetry. In the absence of *Nodal*, we show that some degree of asymmetric morphogenesis occurs, as reported also upon bilateral expression of *Nodal*, in *Snail* mutants (Murray and Gridley, 2006). This is in agreement with the existence of a generator of asymmetry that is independent of the Nodal left-right bias. We had shown previously that heart looping can be reproduced by a buckling mechanism, when the heart tube grows between fixed poles (Le Garrec et al., 2017). Disruption of buckling, when heart tube growth is impaired, leads to straight tubes, as exemplified in *Tbx20* or *Nkx2-5* mutants (Lyons et al., 1995; Stennard et al., 2005). Computer simulations show that the buckling mechanism in isolation generates random deformations, whereas small left-right asymmetries at the tube poles are sufficient to bias them. Our work points to the existence of left-right asymmetries at the heart tube poles, independent of Nodal, which orient the buckling of the heart tube. The nature of these asymmetries remains to be uncovered, whether they are stochastic, trivial differences or whether they are genetically controlled asymmetries. The facts that the mutant heart loops are not a continuous spectrum of random shapes and that pole asymmetries are clearly detectable in *Nodal* mutants, would support the second hypothesis. However, the underlying molecular mechanism remains unknown. For the arterial pole rotation, the asymmetric cell proliferation that we have observed in the heart field from E8.5g depends on Nodal signalling and thus would not fit as a mechanism. More promising would be actomyosin, which was shown to be important for the later phase of heart looping in the fish, independently of Nodal (Noël et al., 2013) or for the rotation of another tube, the fly hindgut (Chougule et al., 2020). Asymmetries preceding that of Nodal are evident in the brain, involving Fgf, Notch or Wnt/ $\beta$ -catenin signalling (see Güntürkün and Ocklenburg, 2017), or in the frog embryo, involving ion channels or cytoskeletal rearrangements (Pai et al., 2017).

For the looping of a tube, such as the embryonic heart, intrinsic and extrinsic mechanisms can intervene, depending on whether the asymmetric determinant acts inside or outside the tube. We show that *Nodal* is transiently required in cardiac precursor cells between E8.5c-e. This supports the idea of an extrinsic role of Nodal for heart looping, i.e. in cells outside the heart tube. Whether there are additional intrinsic determinants of heart looping, e.g. regulating differential growth within the tube, remains to be demonstrated.

*Nodal* expressing cells contribute to the myocardium of the arterial and venous poles, but neither to the left ventricle, nor to the majority of the right ventricle. This is reminiscent of the second myocardial lineage (Meilhac et al., 2004) and is consistent with fate mapping of the left second heart field (Domínguez et al., 2012). Our observations of largely negative ventricles would thus suggest that cells of the first lineage are not sensitive to left-right patterning. Indeed, they are defined first (Meilhac et al., 2004), ingress first in the primitive streak (Lescroart et al., 2014), differentiate earlier (Ivanovitch et al., 2017) and reach the heart region (cardiac crescent) before the node has become a left-right organiser at the late headfold (LHF) stage (Kawasumi et al., 2011) and before the heart field expresses *Nodal* at E8.5c. Thus, the second heart field which provides cells for the elongation of the heart tube, as a pre-requisite of the buckling mechanism, and is patterned by *Nodal* signaling, appears as a driving force of heart looping.

Our quantification of the coverage of the *Nodal-ASE-lacZ* staining suggests a 25% contribution of *Nodal* expressing cells to the heart poles at E9.5. Given the short time window of *Nodal* expression and the perdurance of  $\beta$ -galactosidase a day later, we expect that most of *Nodal* expressing cells in the lateral plate mesoderm are labeled with the *Nodal-ASE-lacZ* transgene, compared to an hypothetical *Nodal-ASE-Cre* transgene, which would induce a delay in the initial activation of a reporter. *Nodal-ASE-lacZ* staining thus provides a 3D map of left derivatives in the looped heart tube. The percentage below 50% raises the questions of whether all left cells in the second heart field express *Nodal*, and/or whether left precursor cells contribute less to the heart tube compared to right cells. The higher proliferation of cells that we detect in the right second heart field, as well as the asymmetric contribution of right versus left grafts in the chick precardiac mesoderm (Stalsberg, 1969) would support the second hypothesis.

Our work provides insight into the left-right patterning of cardiac cells, showing that it is a spatio-temporal dynamic process rather than a single event. We have previously detected opposed and sequential left-right asymmetries at the arterial and venous poles (Le Garrec et al., 2017). We now report molecular left-right patterning of the outflow tract (*Wnt11*) and atria (*Bmp2*), which is defective in *Nodal* and *Pitx2* <sup>$\Delta$ ASE/ $\Delta$ ASE</sup> mutants, consistent with malposition of the great arteries and atrial isomerism at birth. However, these molecular anomalies are not fully penetrant and not predictive of a class of abnormal heart looping. This indicates that left-right asymmetry is regulated independently in the different segments of the heart, for the situs of the atria, the position of the atrioventricular canal, the relative position of the ventricles and the regionalisation of the outflow tract. With more markers of the heart

tube poles identified in our transcriptomic analysis, the molecular signature of the asymmetry of cardiac segments will be refined. Another cardiac asymmetry is the curvature of the outflow tract, arising between E8.5j and E9.5, under the control of Nodal. This curvature is not reproduced in our computer simulations, suggesting that it is not related to the buckling. It is also not correlated with proliferation differences (data not shown), leaving its origin unclear.

In the clinics, heterotaxy is a laterality defect associated with mutations affecting the formation or signalling of the left-right organiser (Guimier et al., 2015). The clinical picture is very variable, in terms of associations of left-right anomalies between different organs or between different heart segments (Desgrange et al., 2019; Lin et al., 2014). Even looking at a single structure such as the atria, the parameters of the anatomy of the appendages and of the connection of the inferior caval vein are not always concordant (Tremblay et al., 2017). This is the basis of debates in the nomenclature of heterotaxy, for the qualification of isomerism (Jacobs et al., 2007). Clinical variability may relate to the fact that left-right asymmetry is regulated independently at different levels, and that Nodal regulates either the initiation or the laterality of asymmetry. The previous focus on the symmetry-breaking event as a binary decision (left, right) has masked the dynamics of left-right patterning. In the future, it will be important to correlate classes of abnormal heart loop shapes with specific congenital heart defects. Quantifications of the contribution of different factors to the fine shape of the heart loop, not just its direction, are expected to provide novel perspectives in understanding the origin of severe congenital heart defects associated with heterotaxy or other types of cardiac chamber misalignment.

## Acknowledgments

We thank V. Benhamo, L. Guillemot, L. Bombardelli, M. Bertrand, A. Murukutla, V. Nikovics, J-P. Mulon, J. Lokmer and C. Cimper for technical assistance, JN. Domínguez for advice in embryo culture, J. Collignon for *Nodal-ASE-lacZ* embryos, H. Hamada and Y. Ikawa for *Pitx2<sup>ΔASE/ΔASE</sup>* embryos, B. Sanketi, TT. Tran, N. Kurpios and J. Martin for *Pitx2c<sup>null/null</sup>* mice and *Pitx2abc<sup>tm1Jfm/ tm1Jfm</sup>* embryos, M. Campione for *Pitx2abc<sup>tm1Sac/tm1Sac</sup>* embryos, L. Robertson for *Nodal<sup>fllox/fllox</sup>* mice, S. Zaffran for *Hoxb1<sup>Cre/+</sup>* mice, the histology and imaging platforms of the SFR Necker, C. Bole-Feysot and O. Alibeu of the Genomics platform, N. Cagnard of the Bioinformatics platform, C. Dicu and the LEAT animal facility. This work was supported by core funding from the Institut Pasteur, state funding from the

Agence Nationale de la Recherche under “Investissementsd’avenir” program (ANR-10-IAHU-01), a grant from the ANR [16-CE17-0006-01] to SMM and the MSD-Avenir fund (Devo-Decode project). AD, SB, TB have benefited from a fellowship of the Fondation Lefoulon-Delalande, the Société Française de Pédiatrie and the Pasteur - Paris University (PPU) International PhD Program respectively ; SMM is an INSERM research scientist.

### Author Contributions

Conceptualization: AD, JFLG, SMM; Methodology: AD, JFLG; Software : JFLG ; Formal Analysis : JFLG, AD ; Investigation: AD, JFLG, SB, TB; Writing - original draft: SMM; Writing - review & editing: AD, JFLG, SMM; Visualization: AD, JFLG, SB ; Supervision: SMM, AD ; Project administration: SMM ; Funding acquisition: SMM, AD.

**Declaration of interests.** The authors declare no competing interests.

### Figure Legends

#### **Figure 1. Tracing cells that have expressed Nodal with the *Nodal-ASE-lacZ* transgene.**

(A) Schematic representation of the stages of heart looping in the mouse. The cardiac crescent forms at E8.5c and bulges at E8.5d, while cardiomyocyte differentiate (orange). The cardiac tube forms at E8.5e and elongates, with the right ventricle visible from E8.5f and the outflow region from E8.5h. At E8.5g, the tube appears tilted on the right side, so that the right ventricle is progressively repositioned (E8.5i) to the right side of the left ventricle (E8.5j). At E9.5 the outflow tract is bent and the arterial/venous poles are closer. (B-H) Brightfield images (B, D, F, H) and 3D images by HREM (C, E, G) of *Nodal-ASE-LacZ* embryos at E8.5e, n=2 (B-C), E8.5j, n=2 (D-E) and E9.5, n=2 (F-H). Ventral views (left panels), transversal (third panel) and sagittal (right panel) sections are shown, with  $\beta$ -galactosidase staining in blue. The orange dotted line outlines the heart tube. Regionalisation of the staining in the outflow tract is schematised on the right (G). The black dotted lines in (H) highlight sharp boundaries between  $\beta$ -galactosidase-positive and negative regions. (I-J) Brightfield image (I) and 3D images by HREM (J) of *Sema3c* ISH (in blue), n=2. (K) Quantification of the  $\beta$ -galactosidase-positive myocardium volume at the indicated stages of heart looping. The low correlation coefficient ( $R^2$ ) indicates a constant fraction at the different stages. Scale bars: 200 $\mu$ m. dLA, dorsal left atrium ; LHF, late headfold stage, l-HF, left heart field ; (l-)OFT, (left) outflow tract ; l-SV, left sinus venosus ; LV, left ventricle ; n, number of observations ;

RV, right ventricle ; sAVC, superior atrio-ventricular canal ; ss, somite stage. See also Movie S1.

**Figure 2. Temporal window of *Nodal* expression and signalling.**

(A) Quantification of *Nodal* and *Lefty2* expression by RT-qPCR in microdissected cardiac regions (dotted lines) at LHF (n=3), E8.5c (n=4), E8.5d (n=5), E8.5e (n=4) and E8.5f (n=4 and 3 respectively). The dotted line indicates the threshold of expression, based on primer efficiency in a reference sample. Means and standard deviations are shown. (B) The experimental design of embryo cultures is schematised, for a drug exposure of 8h (left) or 4h (right). Examples of embryos are shown at the beginning (top panels) and end (middle panels) of the cultures, treated with the inhibitor of Nodal signalling (SB504125) or with the adjuvant (DMSO). ISH of *Pitx2* at the end of the culture is in the lower panels, indicating strong (arrows), reduced (black arrowheads) or absent (white arrowhead) expression in the left lateral plate mesoderm. Bilateral expression in the oral ectoderm (yellow arrowheads) provides a control. (C) Corresponding quantification of *Pitx2* expression, as the ratio between the left and right lateral plate mesoderm (see scheme). \*p-value<0.05, \*\*p<0.01 (one-way ANOVA with a Tukey Kramer post-hoc test compared to DMSO (black) or between treatments (grey), n= 5, 5, 5, 6, 4). The orange dotted line indicates symmetric expression. (D) ISH of *Lefty2* at the end of the culture, with the timing of drug treatment indicated below. (E) Corresponding quantification of *Lefty2* expression. \*\*p<0.01 (one-way ANOVA with a Tukey Kramer post-hoc test compared to DMSO, n= 3 per condition). Scale bars: 200µm. LHF, late headfold stage. LLPM, left lateral plate mesoderm ; LV, left ventricle ; n, number of observations ; RLPM, right lateral plate mesoderm ; RV, right ventricle.

**Figure 3. Classes of looping defects in *Nodal*<sup>flox/nul</sup>;*Hoxb1*<sup>Cre/+</sup> mutants.**

(A) Brightfield images of control and mutant embryos at E9.5. Four classes of looping defects are detected, based on the positions of the right and left ventricles. (B) Equal frequency of the four classes of mutants (p-value= 0.93, chi<sup>2</sup> test, n=56 mutant embryos from 33 litters). (C) Double ISH of *Wnt11* (orange arrowhead), labelling the outflow tract and the right ventricle, and *Bmp2* (green arrowhead) labelling the superior atrio-ventricular canal and the ventral left atrium. See also Movie S2-S6 and Figure S1. (D) Principal component (PC) analysis of 33 parameters characterising the loop shape in the different classes of mutants. (E) Clustering of individual mutants based on the four principal components, the values of which is colour coded from blue to orange. Scale bars: 400µm. AVC, atrio-ventricular canal; LA, left atrium;

LV, left ventricle; n, number of observations; OFT, outflow tract; RV, right ventricle; vLA, ventral left atrium. See also Figure S1 and Movies S2-S6.

**Figure 4. Quantification of looping defects in *Nodal*<sup>flox/null</sup>;*Hoxb1*<sup>Cre/+</sup> mutants.**

(A) Cranial views of the 3D segmented heart tube in control and mutants at E9.5, with regions colour-coded based on *Bmp2/Wnt11* expression and histology. The samples are aligned with the notochord vertical. See also Movies S2-S6. (B) The mean trace of the tube axis is represented by a dotted line showing the shape and direction of the heart loop in controls and mutants. The origin (position 0) represents the exit of the outflow tract, seen on a transversal projection (perpendicular to the notochord). Other coloured points are the centres of gravity of the corresponding regions, with an additional point (black) at the interventricular sulcus. The arrow indicates the looping direction, from the venous to the arterial pole. (C) Quantification of the orientation of the RV/LV axis relative to the notochord in controls and the different classes of mutants. Positive (blue) and negative (orange) numbers correspond to the right and left position of the RV respectively. (D) Quantification of the lateral displacement of the venous pole. (E-F) Quantification of the curvature of the outflow tract in the transversal (E) and sagittal (F) planes. Means and standard deviations are shown. \* p-value<0.05, \*\*p<0.01, \*\*\*p<0.001 (Kruskal Wallis test compared to controls, n=11 controls, n=6, 5, 6 and 5 for classes 1, 2, 3 and 4 respectively). See also Figure S2-S3. (G-I) 3D images by HREM of control and mutant embryos. The expression of *Wnt11* and *Bmp2* is in red, the histology in grey. Section planes and the control *Wnt11/Bmp2* pattern are schematised on the right. Regionalisation of the staining in the outflow tract is schematised in the bottom right corner of upper panels. AVC, atrio-ventricular canal; L, left; LV, left ventricle; n, number of observations; OFT, outflow tract; R, right; RV, right ventricle. Scale bars: 200µm. See also Figures S2-S3.

**Figure 5: Simulations of looping defects in *Nodal* mutants by randomized laterality and reduced asymmetry at the heart tube poles.**

(A-C) Superimposition of the mean heart loop shape (see Fig. 4B), seen in a transversal projection, of controls and class 4 *Nodal*<sup>flox/null</sup>;*Hoxb1*<sup>Cre/+</sup> mutants (A), and of mirror imaged control hearts and class 1 mutants (B). The exit of the outflow tract is taken as a landmark for the alignment. The optimised alignment was obtained by sequential rotations around the three axes as indicated. (C) Quantification of the misalignment, as the total distance between the mutant and control landmark positions. (D) Computer simulations of heart looping, with different input conditions. The control simulations are run with a 25° rotation of the arterial

pole (arrow) and a 2.8 fold asymmetric growth at the venous pole (arrowhead). In mutant simulations, the parameters were reduced by half (see the reduced size of arrows and arrowheads). In simulated class 1, asymmetries at the arterial and venous poles were reversed, in simulated class 2 only the venous pole asymmetry was reversed, in simulated class 3 only the arterial pole asymmetry was reversed. The RV/LV axis is marked by a dotted red line, joining the centroids of the two regions. (E) Correlation ( $R^2$ , Pearson coefficient) between the observed and simulated RV/LV axes (n=11 controls, n=6, 5, 6 and 5 for classes 1, 2, 3 and 4 respectively). Means and standard deviations of the observed values are plotted (see Fig. 4C). LV, left ventricle; NO, no optimisation ; AO, alignment optimisation ; RV, right ventricle.

**Figure 6: Nodal targets modulating cell proliferation and differentiation.**

(A) Outline (blue) of the region isolated for RNA-sequencing at E8.5e-f. (B) Normalised sequence counts of genes associated with the cell cycle, differentially expressed (fold change 1.2) in control (n=4) and *Nodal* mutant (n=3) samples. \*p-value<0.05, \*\*\*p<0.001 (DESeq2). Whisker plots show the median, 25th, 75th quartiles (boxes) and the extreme datapoints (whiskers). See also Table S1. (C) Whole mount immunofluorescence of the heart field marker *Isl1* and the mitotic marker Phospho-histoneH3 (P-HH3) in controls and mutants. White arrowheads point to double positive cells. L, left; R, right. Scale bar: 200 $\mu$ m. (D) Quantification of cell proliferation in the right and left heart field in control (n=4, 3, 4, 4, 4 at E8.5e, f, g, h, i respectively) and mutant (n=1, 1, 1, 3, 2 at E8.5e, f, g, h, i respectively) embryos at the indicated stages of heart looping. Means, standard deviations and confidence intervals (CI) are shown for control samples. Proliferation ratios significantly deviate from 1 in control samples from the E8.5f stage, indicating proliferation asymmetry. Proliferation rates are not significantly different from a homogenous distribution between the left and right in any mutant sample ( $\chi^2$  test of homogeneity). (E) Normalised sequence counts of genes associated with cardiomyocyte differentiation, in control (n=4) and mutant (n=3) samples. \*p-value<0.05 (DESeq2). (F) Bootstrap statistical analysis to compare the fold change in the expression of 112 cardiomyocyte genes (red), between controls and mutants, with that of 1,000 randomly sampled sets of 112 genes. The mean fold change for cardiomyocyte genes (0.87) lies 17 standard deviations away from the mean of randomly sampled sets (1.01), indicating a globally significant downregulation of genes involved in cardiomyocyte differentiation. See also Table S2. (G) Brightfield images (left column) and 3D images by HREM (right columns) of *Tnnt1* ISH in control (upper line) and mutant (lower lines) samples at E9.5. The mutant class is indicated in the bottom (n= 1, 3, 2, 3 for classes 1, 2, 3 and 4 respectively). Filled and empty arrowheads point to high and low expression in the inner

curvature of the outflow tract (white) and left atrium (green) respectively. Note that *Tnnt1* expression is bilateralised in the atria of class 2-3 *Nodal* mutants. (H) *Vsnl1* ISH in control (upper line) and mutant (lower lines) samples at E9.5. Filled and empty arrowheads point to high and low expression in the atria (green) respectively. The mutant class is indicated in the bottom (n= 1, 2, 2, 3 for classes 1, 2, 3 and 4 respectively) LA, left atrium; OFT, outflow tract; PE, proepicardium; RA, right atrium. Scale bars: 400µm. See also Figures S4-S5 and Tables S1-S3.

### Figure 7: Nodal targets related to the extracellular matrix.

(A) Normalised sequence counts of genes associated with the extracellular matrix, differentially expressed (fold change 1.2) in control (n=4) and mutant (n=3) samples. \*p-value<0.05, \*\*p<0.01 (DESeq2). Whisker plots show the median, 25th, 75th quartiles (boxes) and the extreme datapoints (whiskers). (B) Brightfield images (upper line) and 3D images by HREM (lower lines) of *Tnc* ISH in control (left column) and mutant (right columns) samples at E9.5 (n=2 in each mutant class). Filled and empty arrowheads point to high and low expression respectively, in the outflow tract (red), heart precursors (orange) and proepicardium (blue). (C, E) *Mmp9* (C) and *Col5a2* (E) expression detected by whole mount RNAscope ISH at E8.5g-h. Filled and empty white arrowheads point to high and low expression respectively, in the heart field and myocardium. Asterisk, blood autofluorescence. (D, F) Corresponding quantification of asymmetric expression in controls and mutants. \*\*p<0.01 (student t-test compared to controls, n=5 controls, 4 mutants for *Mmp9* and n=3 controls, 6 mutants for *Col5a2*). The orange dotted line indicates symmetric expression. Signal in the endocardium (e) is not quantified. (G) Co-expression of *Pitx2* and *Mmp9* in the left outflow tract (outline) by whole mount RNAscope ISH at E9 (n=1). CpM, cardiopharyngeal mesoderm ; L, left ; LV, left ventricle; PaM, paraxial mesoderm ; R, right ; RV, right ventricle. Scale bars: 400 (B), 100 (C, E, G) µm. See also Table S3.

## STAR METHODS

### 1. KEY RESOURCES TABLE

REAGENT or RESOURCE	SOURCE	IDENTIFIER
Antibodies		
Isl1 and Isl2 homeobox	DSHB	39.4D5
Recombinant Anti-Histone H3 (phospho S10 + T11) antibody	Abcam	ab32107
Phospho-Smad2 (Ser465/467) Rabbit mAb	Cell Signaling	3101



Goat anti-rabbit Alexa Fluor 546 secondary antibody	ThermoFisher scientific	A11035
Goat anti-mouse IgG2b Alexa Fluor 488 secondary antibody	ThermoFisher scientific	A21141
Streptavidin Alexafluor conjugated 546	Invitrogen	S11225
Hoechst 33342	Life Technologies	H3570
Chemicals, Peptides, and Recombinant Proteins		
SB 505124, ALK5 inhibitor	Abcam	ab144402
Critical Commercial Assays		
JB-4 embedding kit	Polysciences	00226-1
RNeasy micro kit	Qiagen	74004
Reverse transcription kit	Qiagen	205311
Universal Plus mRNA-seq kit	Nugen	0508-96
RNAscope multiplex fluorescent detection Kit	Biotechne (ACD)	323110
TSA cyanine 5 reagent pack	Akoya Biosciences	SAT704A001EA
Deposited Data		
GEO submission GSE148123	NCBI	GSE148123
Experimental Models: Organisms/Strains		
Mouse: Wild-type C57Bl6J	Jackson	MGI:3028467
Mouse: <i>Nodal</i> <sup>fl/fl</sup>	Lu and Robertson, 2004	MGI:3056345
Mouse: Nodal-ASE-LacZ	Norris et al., 1999	
Mouse: <i>Hoxb1</i> <sup>Cre/+</sup>	Arenkiel et al., 2003	MGI:2668513
Mouse: <i>Pitx2</i> <sup>ASE</sup>	Shiratori et al., 2006	MGI:3767234
Mouse: <i>Pitx2c</i> <sup>null/null</sup>	Liu et al., 2002	MGI:2445428
Mouse: <i>Pitx2abc</i> <sup>tm1Sac/tm1Sac</sup>	Gage et al., 1999	MGI:1857844
Mouse: <i>Pitx2abc</i> <sup>tm1Jfm/tm1Jfm</sup>	Lu et al., 1999	MGI:2136268
Oligonucleotides		
Nodal reverse primer CCTGACTCAAAACCCAAGGC	This paper.	N/A
Nodal forward primer ATTCCAGCAGTTGAGGCAGA	This paper.	N/A
Nodal forward primer CCACCCAATTTCTAGCCCAG	This paper.	N/A
Mouse Tnnt1 antisense riboprobe generation Fwd: 5' to 3' GGTCAAGGCAGAACAGAAGC	This paper.	N/A
Mouse Tnnt1 antisense riboprobe generation Rev+T7: 5' to 3' TAATACGACTCACTATAGCTCCACACAGCAGGTCAT GT	This paper.	N/A
Mouse Tnc antisense riboprobe generation Fwd: 5' to 3' CTACCATCGCCACCAAGTTT	This paper	N/A
Mouse Tnc antisense riboprobe generation Rev+SP6: 5' to 3' ATTTAGGTGACACTATAGATTCTTCTCTGCGGTCTC CA	This paper	N/A
Mouse Nodal primer for RTqPCR Fwd: 5' to 3' GGCAACGCCGACATCATTG	This paper.	N/A
Mouse Nodal primer for RTqPCR Rev: 5' to 3' CAGCAGGCTCTGGATGTAGG	This paper.	N/A
Mouse Pitx2c primer for RTqPCR Fwd: 5' to 3' GAGGTGCATACAATCTCCGATA	This paper.	N/A
Mouse Pitx2c primer for RTqPCR Rev: 5' to 3' TGCCGCTTCTTCTTGGAC	This paper.	N/A
Mouse Lefty2 primer for RTqPCR Rev : 5' to 3' CACAATTGCCTTGAGCTCCGTAGTC	This paper.	N/A

Mouse Lefty2 primer for RTqPCR Fwd : 5' to 3' ATCGACTCTAGGCTCGTGTCATC	This paper.	N/A
Mouse Pitx2ab primer for RTqPCR Rev: 5' to 3' ACTTGGCACCCCTCAAGATCC	This paper.	N/A
Mouse Pitx2ab primer for RTqPCR Fwd: 5' to 3' CTCCATTCCCGGTTATCGGC	This paper.	N/A
RNAscope probe Mm-Col5a2-O1	Biotechne (ACD)	538021
RNAscope probe Mm-Mmp9	Biotechne (ACD)	315941
<b>Recombinant DNA</b>		
pBSSK-Bmp2		Gift from C. Vesque, Developmental Biology Laboratory, IBPS
pBSSK-Lefty2	Sajoh et al., 1999	Gift from J. Collignon, Institut Jacques Monod
pBSSK-Pitx2	L'Honoré et al., 2007	Gift from J. Drouin, IRCM
pBKCMV-Sema3c	Feiner et al., 2001	Gift from R. Kelly, IBDM
pYXASC-Vsnl1	Ola et al., 2012	Gift from H. Sariola, Developmental biology, University of Helsinki
pWnt11		Gift from S. Evans, UCSD
<b>Software and Algorithms</b>		
ImageJ/Fiji	Schindelin et al., 2012	RRID:SCR_002285
Imaris	Bitplane	RRID:SCR_007370
Icy	de Chaumont et al., 2012	RRID:SCR_010587
Gftbox algorithm Matlab Finite Element Analysis package simulating biological growth	Kennaway et al., 2011 Le Garrec et al., 2017	<a href="http://cmpdartsvr3.cmp.uea.ac.uk/wiki/BanhamLab/index.php/Software">http://cmpdartsvr3.cmp.uea.ac.uk/wiki/BanhamLab/index.php/Software</a>
ClustVis	Metsalu and Vilo, 2015	RRID : SCR_017133
Matlab	The Mathworks	RRID: SCR_001622
R	R Project for Statistical Computing	RRID: SCR_001905
Fuzznuc	EMBOSS-MS software	
Prism	Graphpad	RRID: SCR_002798

## **2. RESOURCE AVAILABILITY**

### **Lead contact**

Further information and requests for resources and reagents should be directed to and will be fulfilled by the Lead Contact, Sigolène M. Meilhac (sigolene.meilhac@institutimagine.org)

### **Material availability**

This study did not generate new unique reagents.

All stable reagents generated in this study are available from commercial sources or the Lead Contact without restriction

**Data and Code availability**

The RNAseq dataset generated during this study is available at the NCBI Gene Expression Omnibus (GEO) database with the accession number GSE148123.

The published article includes all code generated or analysed during this study (see Data S1 and Data S2)

**EXPERIMENTAL MODEL AND SUBJECT DETAILS****Animals**

Wild-type mouse embryos were from a C57Bl6J genetic background. The *Nodal-ASE-lacZ* transgenic line (Norris and Robertson, 1999), *Nodal<sup>flox/flox</sup>* (Lu and Robertson, 2004), *Pitx2<sup>ΔASE/ΔASE</sup>* (Shiratori et al., 2006) and *Pitx2c<sup>null/null</sup>* (tm3.1Jfm allele) (Liu et al., 2002) were maintained in a mixed genetic background. The *Pitx2abc<sup>tm1Sac/tm1Sac</sup>* (Gage et al, 1999) line was maintained in C57Bl6/J; the *Pitx2abc<sup>tm1Jfm/tm1Jfm</sup>* (Lu et al, 1999) line was maintained in 129S4/SvJaeS (milder phenotypes) or C57Bl6/J (most severe phenotype) backgrounds. *Nodal<sup>null/+</sup>* mice were generated by crossing *Nodal<sup>flox/flox</sup>* males with *Mef2cAHFCre* transgenic females (Verzi et al., 2005) and then crossed to *Hoxb1<sup>Cre/+</sup>* (Arenkiel et al., 2003). *Nodal<sup>null/+</sup>;Hoxb1<sup>Cre/+</sup>* males were maintained in a mixed genetic background and crossed to *Nodal<sup>flox/flox</sup>* females to generate *Nodal* conditional mutants. Both male and female embryos were collected and used randomly for experiments. Embryonic day (E) 0.5 was defined as noon on the day of vaginal plug detection. Heart looping stages from E8.5c to E8.5j were defined according to the previously published nomenclature (Le Garrec et al., 2017), whereas E8.5a and E8.5b are equivalent to EHF and LHF stages respectively (Downs and Davies, 1993). The number of somites was evaluated from the HREM images. All embryos were genotyped by PCR. For the genotyping of *Nodal* alleles, primers were designed to detect the wild-type (540b), floxed (590b) alleles and deleted allele (1050b). Animals were housed in the Laboratory of Animal Experimentation and Transgenesis of the SFR Necker, Imagine Campus, Paris and in the animal facility of the Institut Pasteur. Animal procedures were approved by the ethical committees of the Institut Pasteur and Paris Descartes and the French Ministry of Research.

**METHOD DETAILS****Embryo culture**

For drug treatment, wild-type E8.5 embryos were collected in Hank's solution. We tested a range of drug concentrations (20-50 $\mu$ M) to avoid toxicity on embryo development and promote efficient *Pitx2* downregulation. A working concentration of 50 $\mu$ M of SB505124 or an equivalent volume of the adjuvant (DMSO) were added to the 75% rat serum, 25% T6 medium, supplemented with 1X Penicillin/Streptomycin. Embryos were cultured with 5% CO<sub>2</sub>, 5% O<sub>2</sub>, in rolling bottles in a precision incubator (BTC Engineering, Milton, Cambridge, UK). At the end of the treatment, embryos were rinsed in PBS and fixed in paraformaldehyde (PFA) 4%. Brightfield images were acquired at the beginning and the end of the culture with a Zeiss AxioCamICc5 Camera and a Zeiss StereoDiscovery V20 stereomicroscope with a Plan Apo 1.0X objective. Drug treatment over 8 hours did not affect overall embryo development, as quantified by the number of newly added somites (3.1 $\pm$ 0.6 and 2.8 $\pm$ 0.5 somites in DMSO (n=8) and SB505124 (n=29) treated embryos respectively, p=0.19, Wilcoxon test).

### **Wholemout $\beta$ -galactosidase staining and immunofluorescence**

Embryos were collected at E8.5 or E9.5. The heart was arrested in diastole with 250mM KCL (E9.5). *Nodal-ASE-LacZ* transgenic embryos were fixed in 4% PFA – 5mM EGTA – 2mM MgCl<sub>2</sub> for 10min. Embryos were then permeabilized in 0.2% NP40 – 2mM MgCl<sub>2</sub> – 0.1% sodium deoxycholate 30min and stained overnight in Xgal solution. Immunofluorescence on whole mount E8.5 embryos was performed after removal of the left headfold as a landmark, using CUBIC clearing as described in (Le Garrec et al., 2017), with Hoechst as a nuclear counterstain. Multi-channel 16-bit images were acquired with a Z.1 lightsheet microscope (Zeiss) and a 20X/1.0 objective. Automatic detection of mitotic cells was performed with the Spots plugin of Imaris and co-localisation with Is11 staining was evaluated manually. Given morphological variations in mutant embryos, their stage of development was evaluated based on the length of the heart tube, using the quantifications of (Le Garrec et al., 2017) as a reference. P-Smad2 staining was adapted from Kawasumi et al, 2011. E8.5 embryos were fixed 2h in 4% PFA, and gradually dehydrated into methanol. We used 3% H<sub>2</sub>O<sub>2</sub> for bleaching before rehydration. Samples were blocked with the TSA Blocking Reagent (Perkin Elmer), incubated with the primary antibody Phospho-Smad2 (1/50) during 48h at 4°C and 4h with the Alexa Fluor conjugated secondary antibody (1/500). Embryos were then cleared in gradually concentrated glycerol before imaging with a fluorescent Stereomicroscope in 80% glycerol.

### **RT-qPCR**

At earlier stages (LHF-E8.5d), cardiogenic regions were isolated as shown in Fig. 2A. From E8.5e, the heart tube was removed. From E8.5c the heart field was bisected to keep the left half only. The posterior boundary is set at the level of the second somite, in agreement with fate maps (Domínguez et al., 2012). At E9.5, embryos were cut into three pieces: “the head” until the second branchial arch, the “heart region” until the proepicardium and depleted from the neural tube, the rest as “the tail”. The tissue was flash frozen in liquid nitrogen. RNAs were extracted in TRIzol-Chloroform and purified using the RNeasy micro kit. Reverse transcription was carried out using the Quantitect Reverse Transcription kit. Quantitative PCR was carried out using a real-time PCR system (BioRad), and primers as listed in the Key Resources Table. *Polr2b* was chosen from the RNA-seq dataset as a reference housekeeping gene, because of its expression in the range of Nodal pathway components (2000 counts), with no variability between samples, including controls and mutants. The mRNA expression levels were measured relatively to *Polr2b* and normalized with a reference cDNA sample (pool of 4 embryos at E8.5c d, g, and j), using the standard  $\Delta\Delta C_t$  method.

### **RNA *in situ* hybridisation**

ISH was performed on wholemount embryos after fixation in PFA 4% and dehydration in methanol 100% following standard protocols. *Lefty2*, *Pitx2*, *Wnt11*, *Bmp2*, *Sema3c*, *Vsnl1* riboprobes were transcribed from plasmids. *Tnc* and *Tnnt1* probes were synthesized by PCR, using primers listed in the Key Resources Table. Hybridization signals were detected by alkaline phosphatase (AP)-conjugated anti-DIG antibodies (1/2500; Roche), which were revealed with NBT/BCIP (magenta) substrate (Roche). After staining, the samples were washed in PBS and post-fixed. Brightfield images were acquired with a Zeiss AxioCamICc5 Camera and a Zeiss StereoDiscovery V20 stereomicroscope with a Plan Apo 1.0X objective. RNAscope ISH was performed with Multiplex Fluorescent v2 Assay (Advanced Cell Diagnostic, cat. no.323110). E8.5 embryos were fixed 24h in PFA at 4% and dehydrated in methanol 100%. The protocol was adapted from (de Soysa et al., 2019). *mm-Col5a2-C1* (Cat No. 538021) and *mm-Mmp9-C1* (Cat No. 315941) probes were used, together with Hoechst as a nuclear counterstain. Amplification steps were performed using the TSA cyanine5 amplification kit (Akoya Bioscience). Samples were then transferred in R2 CUBIC clearing reagents. Multi-channel 16-bit images were acquired with a Z.1 lightsheet microscope (Zeiss) and a 20X/1.0 objective.

### **HREM (High-Resolution Episcopic Microscopy)**

Embryos or hearts were collected and embedded in methacrylate resin (JB4) containing eosin and acridine orange as contrast agents (Le Garrec et al., 2017; Desgrange et al., 2019). One or two channel images of the surface of the resin block were acquired using the optical high-resolution episcopic microscope (Indigo Scientific) and a 1X Apo objective repeatedly after removal of 1.56-1.7  $\mu\text{m}$  (embryos) and 2.34  $\mu\text{m}$  (hearts) thick sections: the tissue architecture was imaged with a GFP filter and the staining of enzymatic precipitates with a RFP filter. The dataset comprises 500-1700 images of 0.96-1.85  $\mu\text{m}$  resolution in x and y depending on the stage. Icy (de Chaumont et al., 2012) and Fiji (ImageJ) softwares were used to crop or scale the datasets. 3D reconstructions were performed with the Fiji plugin Volume Viewer or Imaris (Bitplane).

### **RNA sequencing**

Embryos were microdissected and the tissue was flash frozen in liquid nitrogen. RNA was extracted in TRIzol-Chloroform and purified using the RNeasy micro kit. RNA quality and quantity were assessed using RNA Screen Tape 6000 Pico LabChips with the Tape Station (Agilent Technologies). All RINs were higher than 9.0. The library was established using the Nugen Universal Plus mRNA-Seq kit, using 20 ng of total RNAs as recommended by the manufacturer. The oriented cDNAs produced from the poly-A+ fraction were PCR amplified (15-18 cycles). An equimolar pool of the final indexed RNA-Seq libraries was sequenced on an Illumina HiSeq2500, with paired-end reads of 130 bases and a mean sequencing depth of 58 millions per sample. The RNA-seq data are available in the NCBI Gene Expression Omnibus (GEO) database with the accession number GSE148123.

### **FEA Modeling of the heart tube**

The model is based on the GFtbox finite element analysis software, using a cylindrical mesh, with fixed poles and a dorsal constraint simulating the progressive breakdown of the dorsal mesocardium (Le Garrec et al., 2017). At each successive step during a simulation, each element is deformed according to a growth tensor field specified from the hypotheses of the model.

The control model is based on the following input parameters, chosen to simulate the control shape (Le Garrec et al., 2017) : basic longitudinal growth (2.5%, with a peak value of 5% ventrally between steps 1-40), 25 degrees rightward rotation at the arterial pole (1.1% circumferential growth per step, positive on the left side, negative on the right side), asymmetric longitudinal growth at the venous pole (peak value of 7% on the right, 2.5% on the left), circumferential growth in the ventricles (0.9% in the ventral right ventricle, 0.4% in

the dorsal right ventricle, 1.4% in the left ventricle). Simulations were run for 100 steps. The MATLAB code containing the interaction function of the GFtbox model, and used to generate the control shape in Fig. 6A, is provided in *Data S1*.

The simulations of the mutant shapes were obtained by a 50% reduction in the intensity of the asymmetries at both poles and by simulating the four possible combinations of lateralization at the arterial/venous poles: normal/normal, normal/inverted, inverted/normal and inverted/inverted. The MATLAB code containing the interaction function of the GFtbox model, and used to generate the mutant shapes in Fig. 6A is provided in *Data S2*. This code is edited to run the inverted/inverted combination ("Class 1"), the alternative codes for each of the three other combinations being included as commented lines under the headings "Class 2-4".

### **Phenotyping at perinatal stages**

The situs and anatomy of visceral organs were evaluated by micro-CT imaging (Quantum FX, perkin Elmer) after 72h of Lugol staining (Desgrange et al., 2019). The heart structure was phenotyped on 3D reconstruction of HREM images, based on the segmental approach (Van Praagh, 1972).

## **QUANTIFICATION AND STATISTICAL ANALYSIS**

### **Quantification of the proportion of $\beta$ -galactosidase staining**

Hearts were segmented from HREM images using the IMARIS software (Bitplane). The contour of the myocardium was manually outlined at regular Z intervals of the GFP channel, and the Create Surface function was used to reconstruct the 3D surface. Signal of the  $\beta$ -galactosidase staining intersecting with the myocardium was obtained using the "mask selection" function to extract a new channel and create another 3D surface. The volume of each surface was extracted and the proportion of the stained myocardium was calculated.

### **Quantification of the ISH signal**

Brightfield images were transformed into 8 bit images and black and white were inverted. Two Regions of Interest (ROIs) were drawn, around the right and left lateral plate mesoderm, as schematized in Fig. 2C. The average intensity signal of each ROI was used to calculate the left/right ratio.

### **Quantification of immunofluorescence and RNAscope ISH signal**

The cardiac region was segmented in the 3D lightsheet images using the IMARIS software (Bitplane). The heart/myocardium and heart field were manually outlined at regular intervals of the Hoechst channel and the Create surface function was used to reconstruct the 3D surface. The headfolds and second somite were used as cranial and caudal boundaries of the heart field respectively. This surface was bisected, using the notochord as a midline reference for the heart field, to extract the P-HH3, Mmp9 or Col5a2 channels on the left and right sides. We used the Spot Detector tool to count the number of mitotic cells or RNA molecules and calculate the left/right ratio.

### **3D rendering and visualisation**

We used Fiji Volume Viewer plugin to assess *in situ* labeling within the heart tube in 3D. In parallel we segmented the myocardium from HREM using the IMARIS software (Bitplane). This 3D surface was used to extract the RFP channel corresponding to *in situ* signal within the object. The extracted signal was used to automatically generate a corresponding 3D surface.

### **Quantification of the geometry of the heart loop**

From the 3D reconstruction of the myocardium contour, the axis of the cardiac tube was extracted, using eight landmarks along the length of the tube. Three of these landmarks were obtained with the IMARIS Oblique Slicer function intersecting the tube perpendicularly, and by computation of the centroid of the polygon (MATLAB geom3d library : function `polygonCentroid3d`) : one at the exit of the outflow tract, one at the sulcus between the two ventricles, and one at the bifurcation of the two atria. The five other landmarks were obtained by sub-division of the volume into the outflow tract (positive for *Wnt11*), the right ventricle (without cushions), the left ventricle, the atrio-ventricular canal and left atrium (positive for *Bmp2*) and the right atrium. The center of gravity of each of these volumes was computed, using IMARIS.

The 3D coordinates of the eight landmarks were used to draw the loop of the tube axis as shown in Fig. 4. All the hearts were aligned so that the notochord coincides with the Z axis, and the dorsal-ventral axis with the X axis. This alignment was performed using two landmarks on the notochord and two landmarks defining the bisectrix of the neural groove, then applying two successive 3D rotations to the axis coordinates, using an in-house MATLAB code: first a rotation aligning the notochord with the Z axis, then a rotation aligning the dorsal-ventral axis with the X axis. All measurements shown in Fig. 4 were done on these alignments and averaged for all analysed samples (n indicated in Fig. 4A). The



orientation of the RV/LV axis relative to the notochord, the distance of the venous pole (taken as the bifurcation of the tube) relative to the notochord, the distance between the poles and the tube length, the rotation of the tube at E8.5f were calculated as in Le Garrec et al., 2017. The OFT angles were directly measured on the aligned loops after projection on the indicated planes (transversal : XY; sagittal : XZ). E8.5f *Nodal* mutants in Fig. S3C were classified as rightward or leftward depending on the number of asymmetric points in the arterial half of the heart tube (from 75 $\mu$ m after the bifurcation).

Superimposition of the loops shown in Fig. 5 was obtained by optimization of composite 3D rotations (combining rotations around the three coordinate axes) of the mutant loops relative to the control loop. The 3 basic rotation matrices were each successively incremented by 1° and combined in alternative order (because of non-commutation) to explore the full space of 3D rotations around the exit of the outflow tract taken as a fixed point. Optimization was obtained by minimizing the sum of the euclidean distances between each of the seven mutant landmarks and the corresponding control landmarks. The computations were implemented in MATLAB.

Quantifications of the rotation of the arterial pole and the left displacement of the venous pole at E8.5 were performed as described in Le Garrec et al., 2017 from HREM and lightsheet images respectively.

### **Principal Components Analysis and clustering**

A Principal Components Analysis was performed on 33 variables describing the heart loop in 22 *Nodal* conditional mutants. All segmented hearts were registered, using the exit of the outflow tract as origin, the notochord as Z-axis, and the dorsal-ventral axis as X-axis. The variables are the X, Y, and Z coordinates of 6 landmarks along the loop (outflow tract, right ventricle, inter-ventricular sulcus, left ventricle, atrio-ventricular canal/left atrium, right atrium -see Fig. 4A), as well as the angles between the 5 segments defined by these landmarks and projected on the 3 planes perpendicular to the embryonic axes (dorsal-ventral, cranial-caudal, left-right). Variance scaling was applied by dividing the coordinate variables by the ratio between their average standard deviation and the average standard deviation of the angular variables. The covariance matrix and its diagonalization were then computed with Matlab. The 4 highest eigenvalues, cumulatively accounting for 85% of the total variance, were retained together with their eigenvectors for clustering, using the ClustVis R-package (Metsalu and Vilo, 2015), with correlation distance and average linkage.

### **Bioinformatics analyses of the RNA sequences**

FASTQ files were mapped to the ENSEMBL [Mouse GRCm38] reference using Hisat2 and counted by featureCounts from the Subread R package. Read count normalisations and group comparisons were performed by three independent and complementary statistical methods: DESeq2, edgeR and LimmaVoom. Flags were computed from counts normalized to the mean coverage. All normalized counts  $<20$  were considered as background (flag 0) and  $\geq 20$  as signal (flag=1). P50 lists used for the statistical analysis regroup the genes showing flag=1 for at least half of the compared samples. Unsupervised cluster analysis was performed by hierarchical clustering using the Spearman correlation similarity measure and average linkage algorithm. The results of the three methods were filtered for differentially expressed genes between control and mutant samples, on the basis of a p-value lower than 0.05 and a fold change greater than 1.2. Functional analyses were carried out using the Gene Ontology database (PANTHER Overrepresentation test).

### **Bioinformatics analysis of ASE elements**

The analysis was performed as described in Guzman-Ayala et al., 2009 on the Ensembl GRCh38 mouse reference genome (48,526 genes). *Nodal*, *Lefty2* and *Pitx2* were used as positive controls.

### **Bootstrap inference on transcriptomic data**

In order to assess how significantly genes of cardiomyocyte differentiation deviate from the average gene expression fold change between control and mutant samples, a bootstrap method was applied. The analysis was restricted to the 9,375 genes with a minimum of 150 normalised counts (see Fig. S5B). 112 were selected as cardiomyocyte differentiation, because they encode sarcomere components, ion channels, transcription factors, adhesion proteins or signals required for cardiomyocyte differentiation, or on the basis of previous RNA-seq datasets (DeLaughter et al., 2016; Li et al., 2016). The 9,375 genes were resampled 1,000 times, with replacement, into sub-samples of 112 genes (MATLAB RandStream method using the Mersenne twister generator). The means and standard deviations of the fold change distribution between mutant and control embryos for these 1,000 bootstrap samples were assessed, and compared to the mean and standard deviation for the 112 genes of cardiomyocyte differentiation.

### **Statistical analysis**

Sample size was checked post-hoc, using the calculator [powerandsamplesize.com](http://powerandsamplesize.com), in order to ensure a power of at least 0.8, with a type I error probability of 0.05, with an effect size of

20%. The collection of full litters was used to randomise imaging experiments. Group allocation was based on PCR genotyping. 3 outliers were excluded from geometric analysis based on a lower number of somites (Fig. 4 and S2). One mutant sample was discarded from the RNA-seq analysis because of a poor gene coverage. All sample numbers (n) indicated in the text refer to biological replicates, i.e. different embryos. Investigators were blinded to allocation during imaging and phenotypic analysis, but not during quantifications. Tests were performed with Excel and R. The correlation between two data series was quantified by the square of the Pearson coefficient  $R^2$ . The regression line was computed using the least square method. Comparisons of two centre-values were done on the average, or the geometrical mean when ratios were compared, using a Student two-tailed test. When more than two centre-values were compared, an ANOVA was calculated, with a Tukey Kramer post-hoc test, unless a normal distribution could not be assumed, in which case a Kruskal Wallis test was used. For comparing left and right angles at successive positions, a paired Student test was used. The 95% confidence intervals for the mean were calculated assuming a normal distribution of measurements. A  $\chi^2$  test was used to evaluate the randomisation of class frequency and the symmetry of proliferation rates between left and right heart precursors.

## References

- Ammirabile, G., Tessari, A., Pignataro, V., Szumska, D., Sutura Sardo, F., Benes, J., Balistreri, M., Bhattacharya, S., Sedmera, D., and Campione, M. (2012). *Pitx2* confers left morphological, molecular, and functional identity to the sinus venosus myocardium. *Cardiovascular Research* 93, 291–301.
- Arenkiel, B.R., Gaufo, G.O., and Capecchi, M.R. (2003). *Hoxb1* neural crest preferentially form glia of the PNS. *Dev. Dyn.* 227, 379–386.
- Bajolle, F., Zaffran, S., Kelly, R.G., Hadchouel, J., Bonnet, D., Brown, N.A., and Buckingham, M.E. (2006). Rotation of the Myocardial Wall of the Outflow Tract Is Implicated in the Normal Positioning of the Great Arteries. *Circulation Research* 98, 421–428.
- Bennett, J.T., Joubin, K., Cheng, S., Aanstad, P., Herwig, R., Clark, M., Lehrach, H., and Schier, A.F. (2007). Nodal signaling activates differentiation genes during zebrafish gastrulation. *Developmental Biology* 304, 525–540.
- Both, von, I., Silvestri, C., Erdemir, T., Lickert, H., Walls, J.R., Henkelman, R.M., Rossant, J., Harvey, R.P., Attisano, L., and Wrana, J.L. (2004). *Foxh1* Is Essential for Development of the Anterior Heart Field. *Developmental Cell* 7, 331–345.
- Bouvagnet, P., and de Bellaing, A.M. (2016). Human Genetics of d-Transposition of the Great Arteries. In *Congenital Heart Diseases: The Broken Heart*, Rickert-Sperling S., Kelly R., Driscoll D., eds. (Springer, Vienna), pp. 439–447.
- Brennan, J., Norris, D.P., and Robertson, E.J. (2002). Nodal activity in the node governs left-right asymmetry. *Genes & Development* 16, 2339–2344.

- Brown, N.A., and Wolpert, L. (1990). The development of handedness in left/right asymmetry. *Development* *109*, 1–9.
- Brown, S., Teo, A., Pauklin, S., Hannan, N., Cho, C.H.H., Lim, B., Vardy, L., Dunn, N.R., Trotter, M., Pedersen, R., et al. (2011). Activin/Nodal Signaling Controls Divergent Transcriptional Networks in Human Embryonic Stem Cells and in Endoderm Progenitors. *Stem Cells* *29*, 1176–1185.
- Campione, M., Ros, M.A., Icardo, J.M., Piedra, E., Christoffels, V.M., Schweickert, A., Blum, M., Franco, D., and Moorman, A.F.M. (2001). Pitx2 Expression Defines a Left Cardiac Lineage of Cells: Evidence for Atrial and Ventricular Molecular Isomerism in the iv/iv Mice. *Developmental Biology* *231*, 252–264.
- Chougule, A., Lapraz, F., Földi, I., Cerezo, D., Mihály, J., and Noselli, S. (2020). The *Drosophila* actin nucleator DAAM is essential for left-right asymmetry. *PLoS Genet* *16*, e1008758.
- Coda, D.M., Gaarenstroom, T., East, P., Patel, H., Miller, D.S.J., Lobley, A., Matthews, N., Stewart, A., and Hill, C.S. (2017). Distinct modes of SMAD2 chromatin binding and remodeling shape the transcriptional response to NODAL/Activin signaling. *eLife Sciences* *6*, 720.
- Collignon, J., Varlet, I., and Robertson, E.J. (1996). Relationship between asymmetric nodal expression and the direction of embryonic turning. *Nature* *381*, 155–158.
- Concha, M.L., Burdine, R.D., Russell, C., Schier, A.F., and Wilson, S.W. (2000). A nodal signaling pathway regulates the laterality of neuroanatomical asymmetries in the zebrafish forebrain. *Neuron* *28*, 399–409.
- DaCosta Byfield, S., Major, C., Laping, N.J., and Roberts, A.B. (2004). SB-505124 is a selective inhibitor of transforming growth factor-beta type I receptors ALK4, ALK5, and ALK7. *Mol. Pharmacol.* *65*, 744–752.
- de Chaumont, F., Dallongeville, S., Chenouard, N., Hervé, N., Pop, S., Provoost, T., Meas-Yedid, V., Pankajakshan, P., Lecomte, T., Le Montagner, Y., et al. (2012). Icy: an open bioimage informatics platform for extended reproducible research. *Nat Methods* *9*, 690–696.
- de Soysa, T.Y., Ranade, S.S., Okawa, S., Ravichandran, S., Huang, Y., Salunga, H.T., Schricker, A., del Sol, A., Gifford, C.A., and Srivastava, D. (2019). Single-cell analysis of cardiogenesis reveals basis for organ-level developmental defects. *Nature* *572*, 120–124.
- DeLaughter, D.M., Bick, A.G., Wakimoto, H., McKean, D., Gorham, J.M., Kathiriya, I.S., Hinson, J.T., Homsy, J., Gray, J., Pu, W., et al. (2016). Single-Cell Resolution of Temporal Gene Expression during Heart Development. *Developmental Cell* *39*, 480–490.
- Desgrange, A., Le Garrec, J.-F., and Meilhac, S.M. (2018). Left-right asymmetry in heart development and disease: forming the right loop. *Development* *145*, dev162776–19.
- Desgrange, A., Lokmer, J., Marchiol, C., Houyel, L., and Meilhac, S.M. (2019). Standardised imaging pipeline for phenotyping mouse laterality defects and associated heart malformations, at multiple scales and multiple stages. *Dis Model Mech* *12*, dmm038356–13.
- Domínguez, J.N., Meilhac, S.M., Bland, Y.S., Buckingham, M.E., and Brown, N.A. (2012). Asymmetric fate of the posterior part of the second heart field results in unexpected left/right contributions to both poles of the heart. *Circulation Research* *111*, 1323–1335.
- Downs, K.M., and Davies, T. (1993). Staging of gastrulating mouse embryos by morphological landmarks in the dissecting microscope. *Development* *118*, 1255–1266.
- Echelard, Y., Vassileva, G., and McMahon, A.P. (1994). Cis-acting regulatory sequences governing Wnt-1 expression in the developing mouse CNS. *Development* *120*, 2213–2224.
- Feiner, L., Webber, A.L., Brown, C.B., Lu, M.M., Jia, L., Feinstein, P., Mombaerts, P., Epstein, J.A., and Raper, J.A. (2001). Targeted disruption of semaphorin 3C leads to persistent truncus arteriosus and aortic arch interruption. *Development* *128*, 3061–3070.

- Forlani, S., Lawson, K.A., and Deschamps, J. (2003). Acquisition of Hox codes during gastrulation and axial elongation in the mouse embryo. *Development* *130*, 3807–3819.
- Furtado, M.B., Biben, C., Shiratori, H., Hamada, H., and Harvey, R.P. (2011). Characterization of Pitx2c expression in the mouse heart using a reporter transgene. *Dev. Dyn.* *240*, 195–203.
- Gage, P.J., Suh, H., and Camper, S.A. (1999). Dosage requirement of Pitx2 for development of multiple organs. *Development* *126*, 4643–4651
- Galli, D., Dominguez, J.N., Zaffran, S., Munk, A., Brown, N.A., and Buckingham, M.E. (2008). Atrial myocardium derives from the posterior region of the second heart field, which acquires left-right identity as Pitx2c is expressed. *Development* *135*, 1157–1167.
- Guimier, A., Gabriel, G.C., Bajolle, F., Tsang, M., Liu, H., Noll, A., Schwartz, M., Malti, El, R., Smith, L.D., Klena, N.T., et al. (2015). MMP21 is mutated in human heterotaxy and is required for normal left-right asymmetry in vertebrates. *Nat Genet* *47*, 1260–1263.
- Guzman-Ayala, M., Lee, K.L., Mavrakis, K.J., Gogolidou, P., Norris, D.P., and Episkopou, V. (2009). Graded Smad2/3 Activation Is Converted Directly into Levels of Target Gene Expression in Embryonic Stem Cells. *PLoS ONE* *4*, e4268–20.
- Güntürkün, O., and Ocklenburg, S. (2017). Ontogenesis of Lateralization. *Neuron* *94*, 249–263.
- Hagos, E.G., and Dougan, S.T. (2007). Time-dependent patterning of the mesoderm and endoderm by Nodal signals in zebrafish. *BMC Dev. Biol.* *7*, 22.
- Ivanovitch, K., Temino, S., and Torres, M. (2017). Live imaging of heart tube development in mouse reveals alternating phases of cardiac differentiation and morphogenesis. *eLife Sciences* *6*.
- Jacobs, J.P., Anderson, R.H., Weinberg, P.M., Walters, H.L., Tchervenkov, C.I., Del Duca, D., Franklin, R.C.G., Aiello, V.D., Béland, M.J., Colan, S.D., et al. (2007). The nomenclature, definition and classification of cardiac structures in the setting of heterotaxy. *Cardiology in the Young* *17 Suppl 2*, 1–28.
- Kaufman, M.H., and Navaratnam, V. (1981). Early differentiation of the heart in mouse embryos. *Journal of Anatomy* *133*, 235–246.
- Kawasumi, A., Nakamura, T., Iwai, N., Yashiro, K., Saijoh, Y., Belo, J.A., Shiratori, H., and Hamada, H. (2011). Left–right asymmetry in the level of active Nodal protein produced in the node is translated into left–right asymmetry in the lateral plate of mouse embryos. *Developmental Biology* *353*, 321–330.
- Kelly, R.G., Brown, N.A., and Buckingham, M.E. (2001). The arterial pole of the mouse heart forms from Fgf10-expressing cells in pharyngeal mesoderm. *Developmental Cell* *1*, 435–440.
- Kennaway, R., Coen, E., Green, A., and Bangham, A. (2011). Generation of diverse biological forms through combinatorial interactions between tissue polarity and growth. *PLoS Comput Biol* *7*, e1002071.
- Kitamura, K., Miura, H., Miyagawa-Tomita, S., Yanazawa, M., Katoh-Fukui, Y., Suzuki, R., Ohuchi, H., Suehiro, A., Motegi, Y., Nakahara, Y., et al. (1999). Mouse Pitx2 deficiency leads to anomalies of the ventral body wall, heart, extra- and periocular mesoderm and right pulmonary isomerism. *Development* *126*, 5749–5758.
- Kumar, A., Lualdi, M., Lewandoski, M., and Kuehn, M.R. (2008). Broad mesodermal and endodermal deletion of Nodal at postgastrulation stages results solely in left/right axial defects. *Dev. Dyn.* *237*, 3591–3601.
- L'Honoré, A., Coulon, V., Marcil, A., Lebel, M., Lafrance-Vanasse, J., Gage, P., Camper, S., and Drouin, J. (2007). Sequential expression and redundancy of Pitx2 and Pitx3 genes during muscle development. *Developmental Biology* *307*, 421–433.
- Le Garrec, J.-F., Domínguez, J.N., Desgrange, A., Ivanovitch, K.D., Raphaël, E., Bangham, J.A., Torres, M., Coen, E., Mohun, T.J., and Meilhac, S.M. (2017). A predictive model of

- asymmetric morphogenesis from 3D reconstructions of mouse heart looping dynamics. *eLife Sciences* 6, e28951–35.
- Lee, J.D., and Anderson, K.V. (2008). Morphogenesis of the node and notochord: The cellular basis for the establishment and maintenance of left-right asymmetry in the mouse. *Dev. Dyn.* 237, 3464–3476.
- Lescroart, F., Kelly, R.G., Le Garrec, J.F., Nicolas, J.F., Meilhac, S.M., and Buckingham, M. (2010). Clonal analysis reveals common lineage relationships between head muscles and second heart field derivatives in the mouse embryo. *Development* 137, 3269–3279.
- Lescroart, F., Mohun, T., Meilhac, S.M., Bennett, M., and Buckingham, M. (2012). Lineage tree for the venous pole of the heart: clonal analysis clarifies controversial genealogy based on genetic tracing. *Circulation Research* 111, 1313–1322.
- Lescroart, F., Chabab, S., Lin, X., Rulands, S., Paulissen, C., Rodolosse, A., Auer, H., Achouri, Y., Dubois, C., Bondue, A., et al. (2014). Early lineage restriction in temporally distinct populations of *Mesp1* progenitors during mammalian heart development. *Nature Cell Biology* 16, 829–840.
- Levin, M., Johnson, R.L., Stern, C.D., Kuehn, M.R., and Tabin, C.J. (1995). A Molecular Pathway Determining Left-Right Asymmetry in Chick Embryogenesis. *Cell* 82, 803–814.
- Li, G., Xu, A., Sim, S., Priest, J.R., Tian, X., Khan, T., Quertermous, T., Zhou, B., Tsao, P.S., Quake, S.R., et al. (2016). Transcriptomic Profiling Maps Anatomically Patterned Subpopulations among Single Embryonic Cardiac Cells. *Developmental Cell* 39, 491–507.
- Lin, C.R., Kioussi, C., O'Connell, S., Briata, P., Szeto, D., Liu, F., Izpisua-Belmonte, J.C., and Rosenfeld, M.G. (1999). *Pitx2* regulates lung asymmetry, cardiac positioning and pituitary and tooth morphogenesis. *Nature* 401, 279–282.
- Lin, A.E., Krikov, S., Riehle-Colarusso, T., Frías, J.L., Belmont, J., Anderka, M., Geva, T., Getz, K.D., Botto, L.D., National Birth Defects Prevention Study (2014). Laterality defects in the national birth defects prevention study (1998–2007): birth prevalence and descriptive epidemiology. *Am. J. Med. Genet. A* 164A, 2581–2591.
- Linask, K.K., Han, M.-D., Linask, K.L., Schlange, T., and Brand, T. (2003). Effects of antisense misexpression of *CFC* on downstream *flectin* protein expression during heart looping. *Dev. Dyn.* 228, 217–230.
- Linask, K.K., Han, M., Cai, D.H., Brauer, P.R., and Maisastry, S.M. (2005). Cardiac morphogenesis: matrix metalloproteinase coordination of cellular mechanisms underlying heart tube formation and directionality of looping. *Dev. Dyn.* 233, 739–753.
- Liu, C., Liu, W., Lu, M.F., Brown, N.A., and Martin, J.F. (2001). Regulation of left-right asymmetry by thresholds of *Pitx2c* activity. *Development* 128, 2039–2048.
- Liu, C., Liu, W., Palie, J., Lu, M.-F., Brown, N.A., and Martin, J.F. (2002). *Pitx2c* patterns anterior myocardium and aortic arch vessels and is required for local cell movement into atrioventricular cushions. *Development* 129, 5081–5091.
- Lowe, L.A., Supp, D.M., Sampath, K., Yokoyama, T., Wright, C.V., Potter, S.S., Overbeek, P., and Kuehn, M.R. (1996). Conserved left-right asymmetry of nodal expression and alterations in murine *situs inversus*. *Nature* 381, 158–161.
- Lowe, L.A., Yamada, S., and Kuehn, M.R. (2001). Genetic dissection of nodal function in patterning the mouse embryo. *Development* 128, 1831–1843.
- Lu, C.C., and Robertson, E.J. (2004). Multiple roles for *Nodal* in the epiblast of the mouse embryo in the establishment of anterior-posterior patterning. *Developmental Biology* 273, 149–159.
- Lu, M.F., Pressman, C., Dyer, R., Johnson, R.L., and Martin, J.F. (1999). Function of *Rieger* syndrome gene in left-right asymmetry and craniofacial development. *Nature* 401, 276–278.

- Lyons, I., Parsons, L.M., Hartley, L., Li, R., Andrews, J.E., Robb, L., and Harvey, R.P. (1995). Myogenic and morphogenetic defects in the heart tubes of murine embryos lacking the homeo box gene *Nkx2-5*. *Genes & Development* 9, 1654–1666.
- Ma, L., Lu, M.-F., Schwartz, R.J., and Martin, J.F. (2005). *Bmp2* is essential for cardiac cushion epithelial-mesenchymal transition and myocardial patterning. *Development* 132, 5601–5611.
- Marques, S., Borges, A.C., Silva, A.C., Freitas, S., Cordenonsi, M., and Belo, J.A. (2004). The activity of the Nodal antagonist *Cerl-2* in the mouse node is required for correct L/R body axis. *Genes & Development* 18, 2342–2347.
- Martin, J.F., Amendt, B.A., and Bronw, N. (2010). *Pitx2* in cardiac left–right asymmetry and human disease. In *Heart Development and Regeneration*, N. Rosenthal, and R.P. Harvey, eds. (Elsevier), pp. 307–322.
- Meilhac, S.M., Esner, M., Kelly, R.G., Nicolas, J.-F., and Buckingham, M.E. (2004). The clonal origin of myocardial cells in different regions of the embryonic mouse heart. *Developmental Cell* 6, 685–698.
- Metsalu, T., and Vilo, J. (2015). ClustVis: a web tool for visualizing clustering of multivariate data using Principal Component Analysis and heatmap. *Nucleic Acids Res.* 43, W566–70.
- Mohapatra, B., Casey, B., Li, H., Ho-Dawson, T., Smith, L., Fernbach, S.D., Molinari, L., Niesh, S.R., Jefferies, J.L., Craigen, W.J., et al. (2008). Identification and functional characterization of NODAL rare variants in heterotaxy and isolated cardiovascular malformations. *Human Molecular Genetics* 18, 861–871.
- Murray, S.A., and Gridley, T. (2006). Snail family genes are required for left-right asymmetry determination, but not neural crest formation, in mice. *Proc. Natl. Acad. Sci. U.S.a.* 103, 10300–10304.
- Noël, E.S., Verhoeven, M., Lagendijk, A.K., Tessadori, F., Smith, K., Choorapoikayil, S., Hertog, den, J., and Bakkers, J. (2013). A Nodal-independent and tissue-intrinsic mechanism controls heart-looping chirality. *Nature Communications* 4, 2754.
- Nonaka, S., Tanaka, Y., Okada, Y., Takeda, S., Harada, A., Kanai, Y., Kido, M., and Hirokawa, N. (1998). Randomization of left-right asymmetry due to loss of nodal cilia generating leftward flow of extraembryonic fluid in mice lacking *KIF3B* motor protein. *Cell* 95, 829–837.
- Norris, D.P., and Robertson, E.J. (1999). Asymmetric and node-specific nodal expression patterns are controlled by two distinct cis-acting regulatory elements. *Genes & Development* 13, 1575–1588.
- Norris, D.P., Brennan, J., Bikoff, E.K., and Robertson, E.J. (2002). The *Foxh1*-dependent autoregulatory enhancer controls the level of Nodal signals in the mouse embryo. *Development* 129, 3455–3468.
- Pai, V.P., Willocq, V., Pitcairn, E.J., Lemire, J.M., Paré, J.-F., Shi, N.-Q., McLaughlin, K.A., and Levin, M. (2017a). *HCN4* ion channel function is required for early events that regulate anatomical left-right patterning in a nodal and lefty asymmetric gene expression-independent manner. *Biology Open* 6, 1445–1457.
- Ola, R., Lefebvre, S., Braunewell, K.-H., Sainio, K., and Sariola, H. (2012). The expression of *Visinin-like 1* during mouse embryonic development. *Gene Expr. Patterns* 12, 53–62.
- Pai, V.P., Willocq, V., Pitcairn, E.J., Lemire, J.M., Paré, J.-F., Shi, N.-Q., McLaughlin, K.A., and Levin, M. (2017b). *HCN4* ion channel function is required for early events that regulate anatomical left-right patterning in a nodal and lefty asymmetric gene expression-independent manner. *Biology Open* 6, 1445–1457.
- Quail, D.F., Siegers, G.M., Jewer, M., and Postovit, L.-M. (2013). The International Journal of Biochemistry & Cell Biology. *International Journal of Biochemistry and Cell Biology* 45, 885–898.

- Roebroek, A.J., Umans, L., Pauli, I.G., Robertson, E.J., van Leuven, F., Van de Ven, W.J., and Constam, D.B. (1998). Failure of ventral closure and axial rotation in embryos lacking the proprotein convertase Furin. *Development* *125*, 4863–4876.
- Roussigne, M., Bianco, I.H., Wilson, S.W., and Blader, P. (2009). Nodal signalling imposes left-right asymmetry upon neurogenesis in the habenular nuclei. *Development* *136*, 1549–1557.
- Saijoh, Y., Adachi, H., Mochida, K., Ohishi, S., Hirao, A., and Hamada, H. (1999). Distinct transcriptional regulatory mechanisms underlie left-right asymmetric expression of lefty-1 and lefty-2. *Genes & Development* *13*, 259–269.
- Saijoh, Y., Oki, S., Ohishi, S., and Hamada, H. (2003). Left–right patterning of the mouse lateral plate requires nodal produced in the node. *Developmental Biology* *256*, 161–173.
- Schindelin, J., Arganda-Carreras, I., Frise, E., Kaynig, V., Longair, M., Pietzsch, T., Preibisch, S., Rueden, C., Saalfeld, S., Schmid, B., Tinevez, J.-Y., White, D.J., et al. (2012). Fiji: an open-source platform for biological-image analysis. *Nat Methods* *9*, 676–682.
- Schweickert, A., Campione, M., Steinbeisser, H., and Blum, M. (2000). Pitx2 isoforms: involvement of Pitx2c but not Pitx2a or Pitx2b in vertebrate left–right asymmetry. *Mechanisms of Development* *90*, 41–51.
- Shiratori, H., Sakuma, R., Watanabe, M., Hashiguchi, H., Mochida, K., Sakai, Y., Nishino, J., Saijoh, Y., Whitman, M., and Hamada, H. (2001). Two-step regulation of left-right asymmetric expression of Pitx2: initiation by nodal signaling and maintenance by Nkx2. *Mol. Cell* *7*, 137–149.
- Shiratori, H., and Hamada, H. (2006). The left-right axis in the mouse: from origin to morphology. *Development* *133*, 2095–2104.
- Shiratori, H., Yashiro, K., Shen, M.M., and Hamada, H. (2006). Conserved regulation and role of Pitx2 in situs-specific morphogenesis of visceral organs. *Development* *133*, 3015–3025.
- Stalsberg, H. (1969). The origin of heart asymmetry: right and left contributions of the early chick embryo heart. *Developmental Biology* *19*, 100–127.
- Stennard, F.A., Costa, M.W., Lai, D., Biben, C., Furtado, M.B., Solloway, M.J., McCulley, D.J., Leimena, C., Preis, J.I., Dunwoodie, S.L., et al. (2005). Murine T-box transcription factor Tbx20 acts as a repressor during heart development, and is essential for adult heart integrity, function and adaptation. *Development* *132*, 2451–2462.
- Théveniau-Ruissy, M., Dandonneau, M., Mesbah, K., Ghez, O., Mattei, M.-G., Miquerol, L., and Kelly, R.G. (2008). The del22q11.2 Candidate Gene Tbx1 Controls Regional Outflow Tract Identity and Coronary Artery Patterning. *Circulation Research* *103*, 142–148.
- Tremblay, C., Loomba, R.S., Frommelt, P.C., Perrin, D., Spicer, D.E., Backer, C., and Anderson, R.H. (2017). Segregating bodily isomerism or heterotaxy: potential echocardiographic correlations of morphological findings. *Cardiology in the Young* *27*, 1470–1480.
- Van Praagh, R. (1972). The segmental approach to diagnosis in congenital heart disease. *Birth Defects Orig. Artic. Ser.* *8*, 4-23.
- Van Praagh, S. (2006). Cardiac malpositions and the heterotaxy syndromes. In Nadas' *Pediatric Cardiology*, J. F. Keane, J. E. Lock and D. C. Fyler, eds., (Philadelphia: Saunders Elsevier Inc.) pp. 589-608.
- Verzi, M.P., McCulley, D.J., De Val, S., Dodou, E., and Black, B.L. (2005). The right ventricle, outflow tract, and ventricular septum comprise a restricted expression domain within the secondary/anterior heart field. *Developmental Biology* *287*, 134–145.
- Vincent, S.D., Norris, D.P., Ann Le Good, J., Constam, D.B., and Robertson, E.J. (2004). Asymmetric Nodal expression in the mouse is governed by the combinatorial activities of two distinct regulatory elements. *Mechanisms of Development* *121*, 1403–1415.



- Yan, Y.T., Gritsman, K., Ding, J., Burdine, R.D., Corrales, J.D., Price, S.M., Talbot, W.S., Schier, A.F., and Shen, M.M. (1999). Conserved requirement for EGF-CFC genes in vertebrate left-right axis formation. *Genes & Development* 13, 2527–2537.
- Zhou, W., Lin, L., Majumdar, A., Li, X., Zhang, X., Liu, W., Etheridge, L., Shi, Y., Martin, J., Van de Ven, W., et al. (2007). Modulation of morphogenesis by noncanonical Wnt signaling requires ATF/CREB family-mediated transcriptional activation of TGF $\beta$ 2. *Nat Genet* 39, 1225–1234.

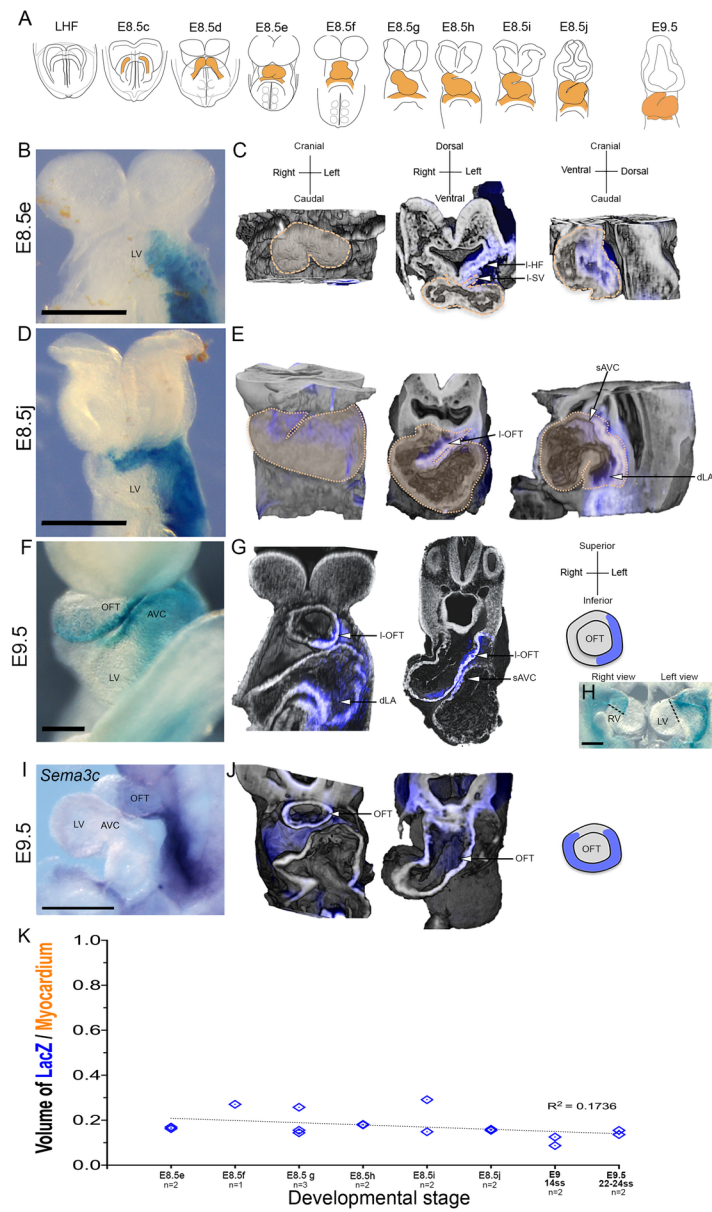
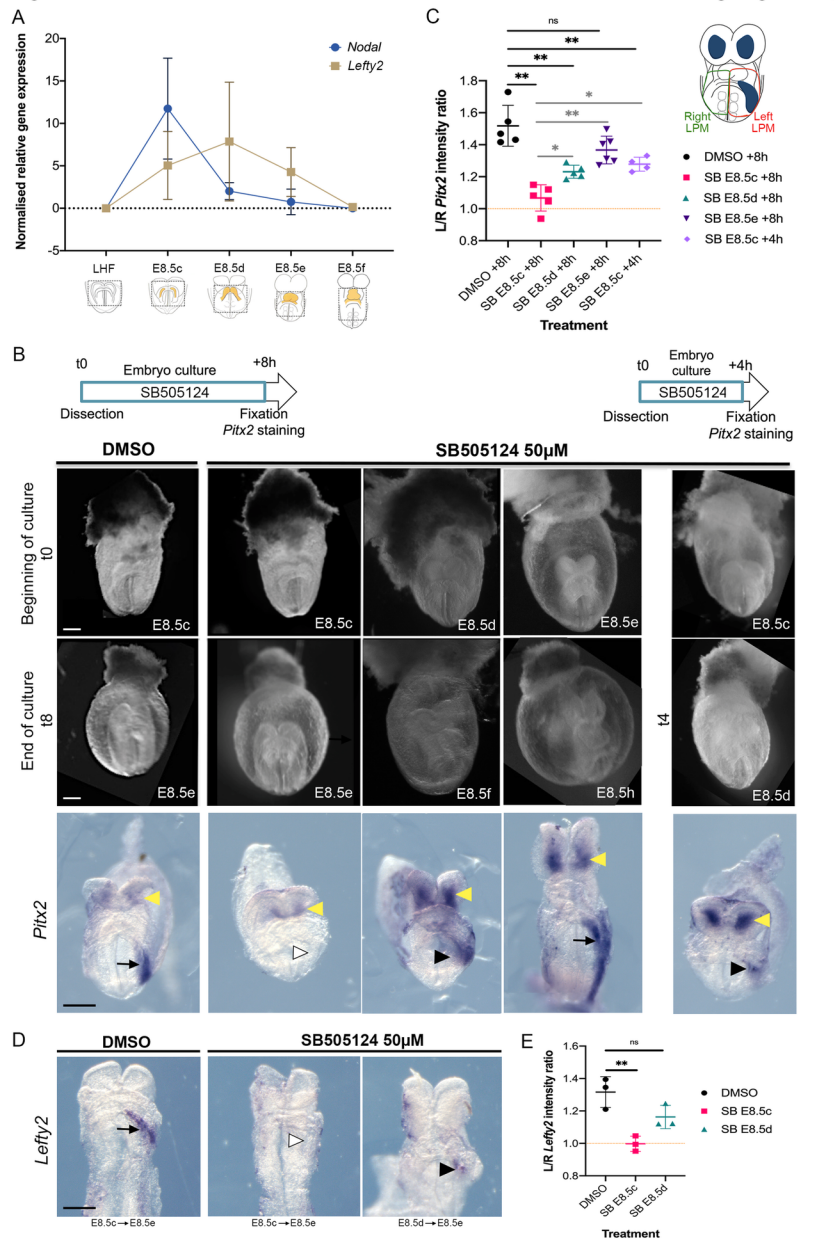
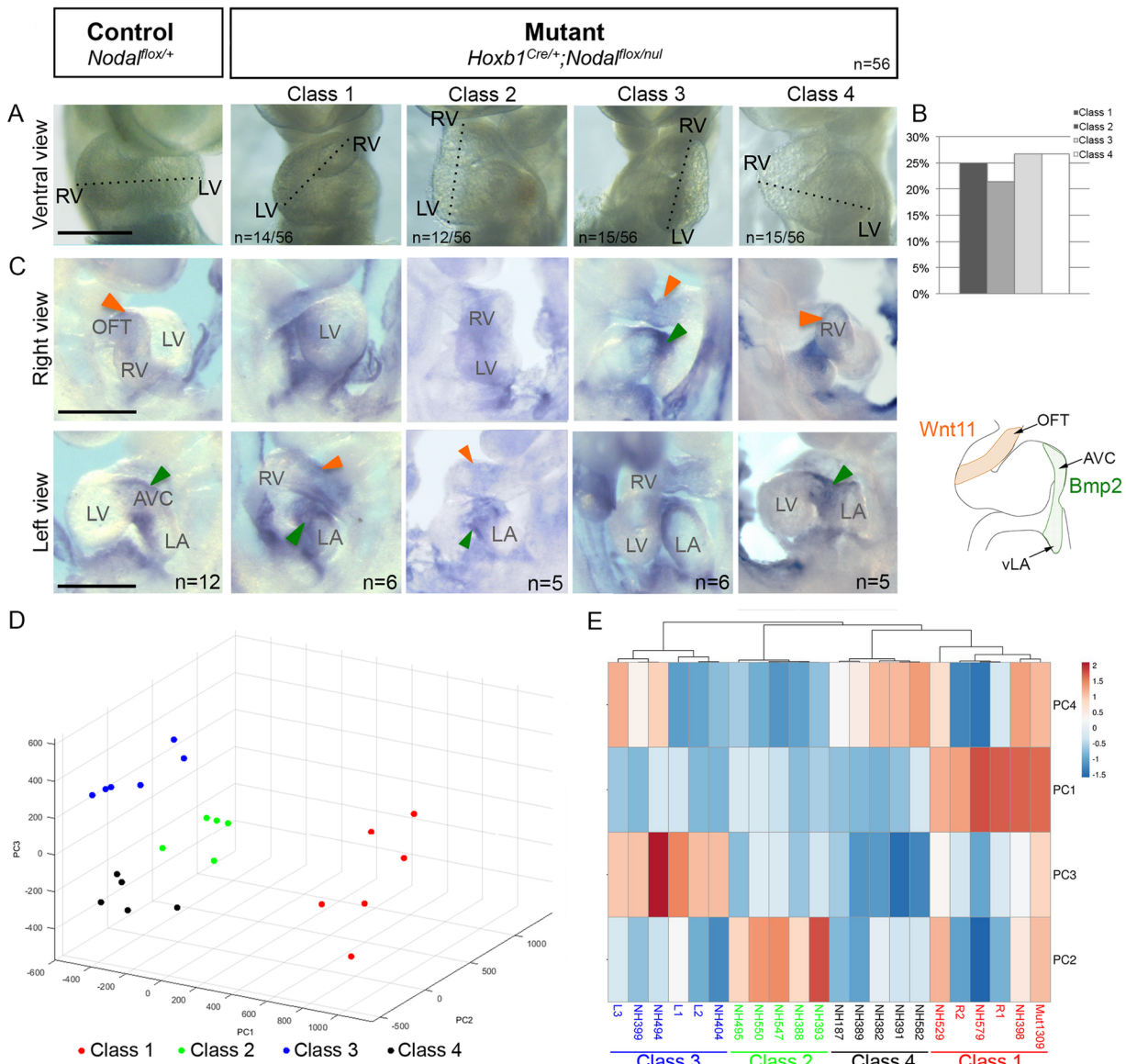


Figure 2





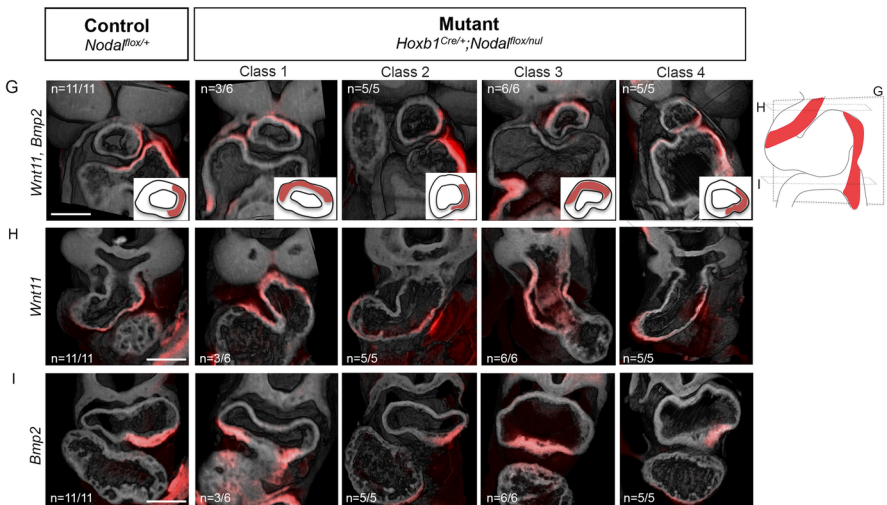
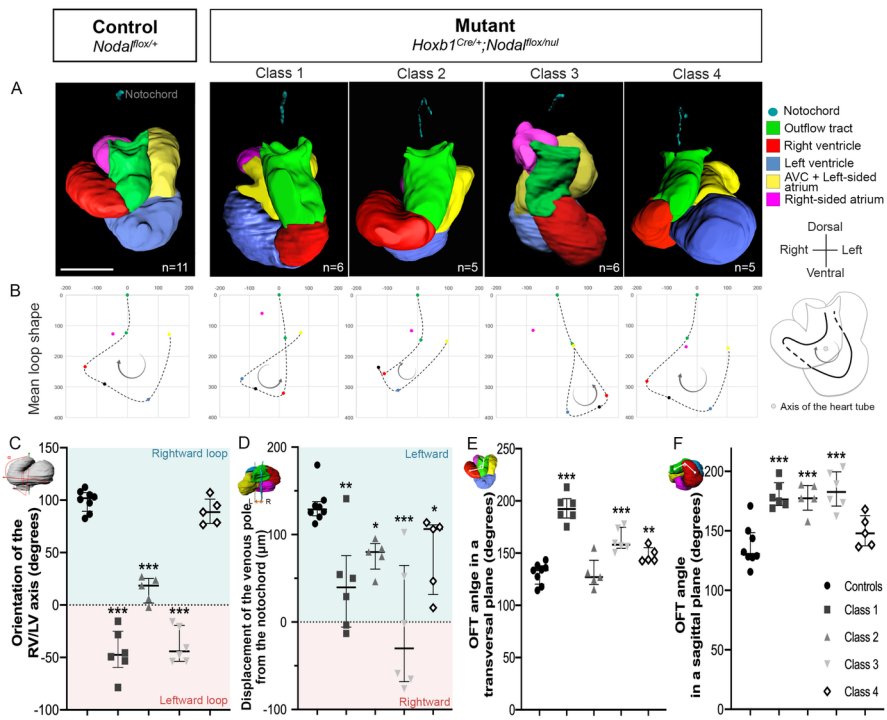
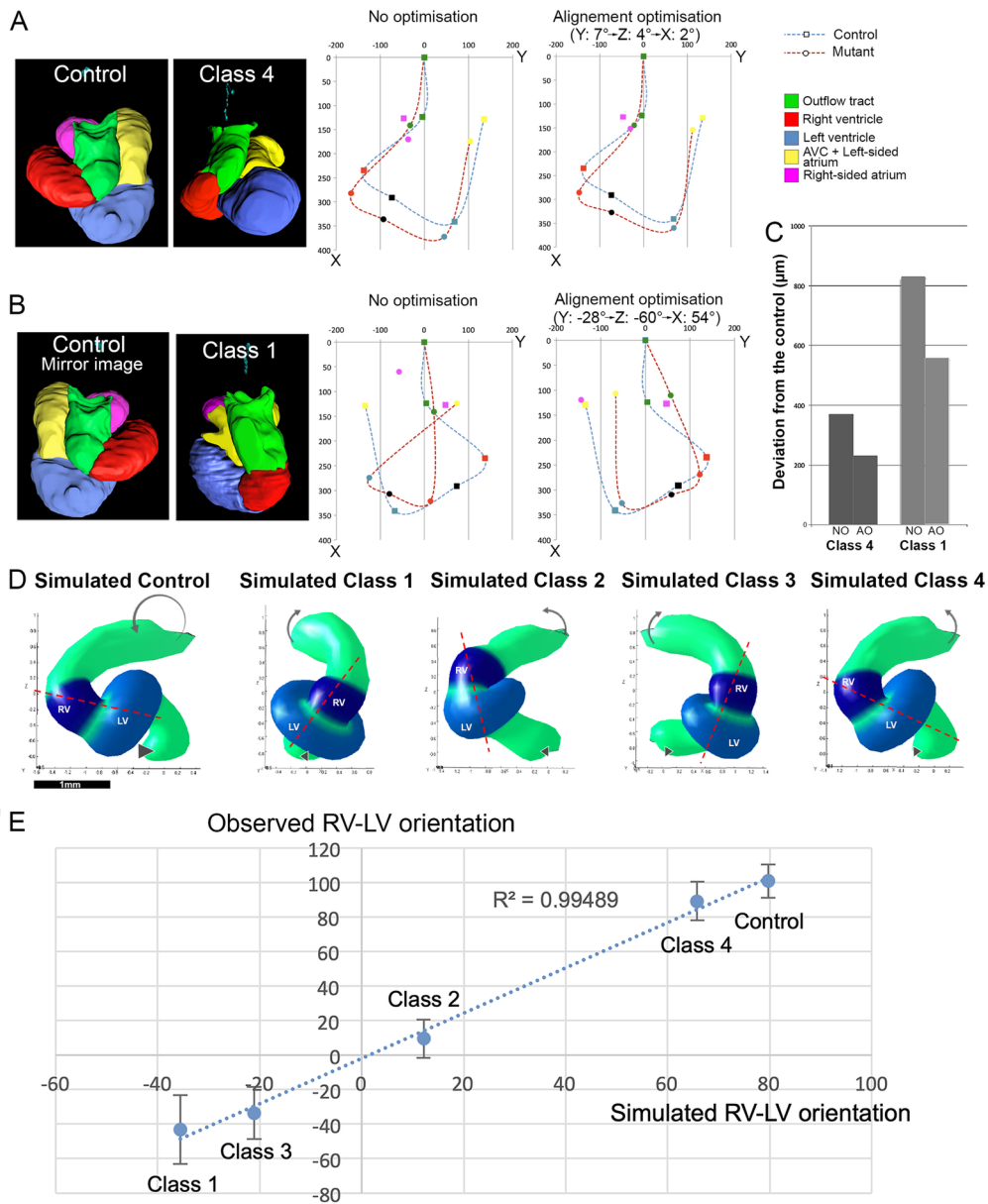
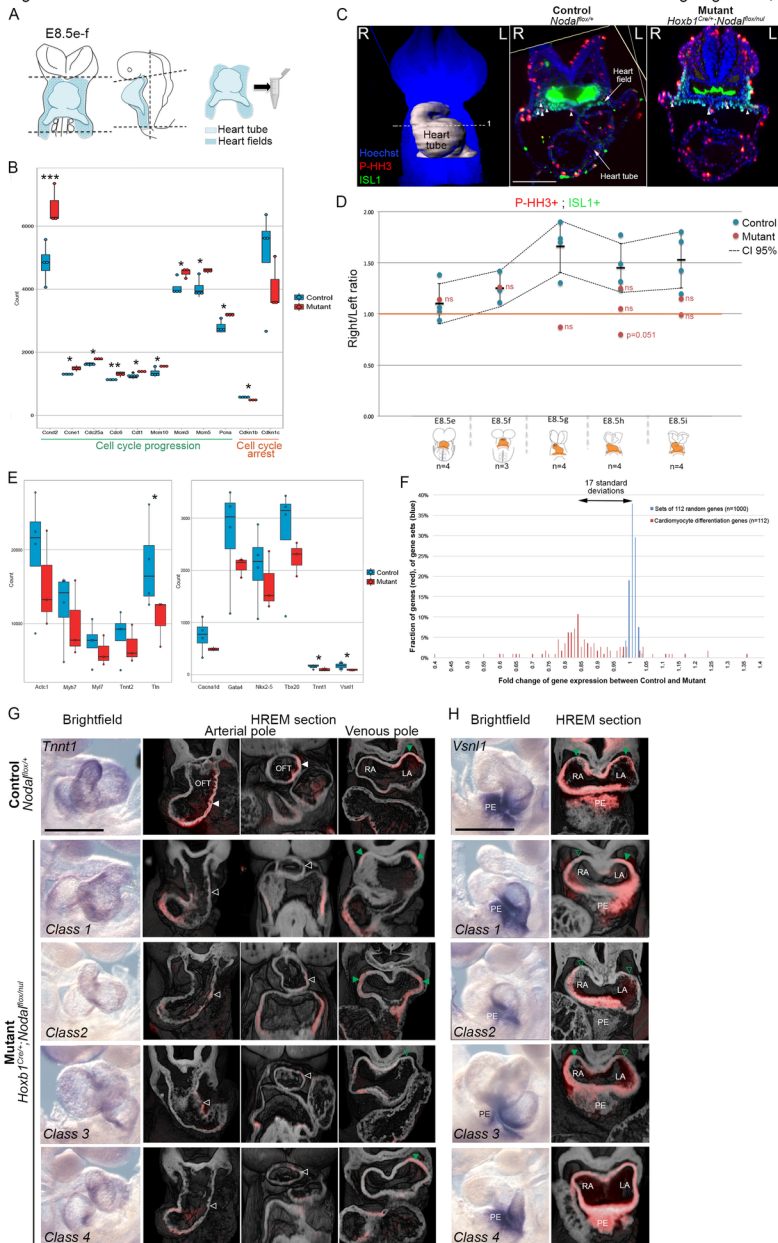
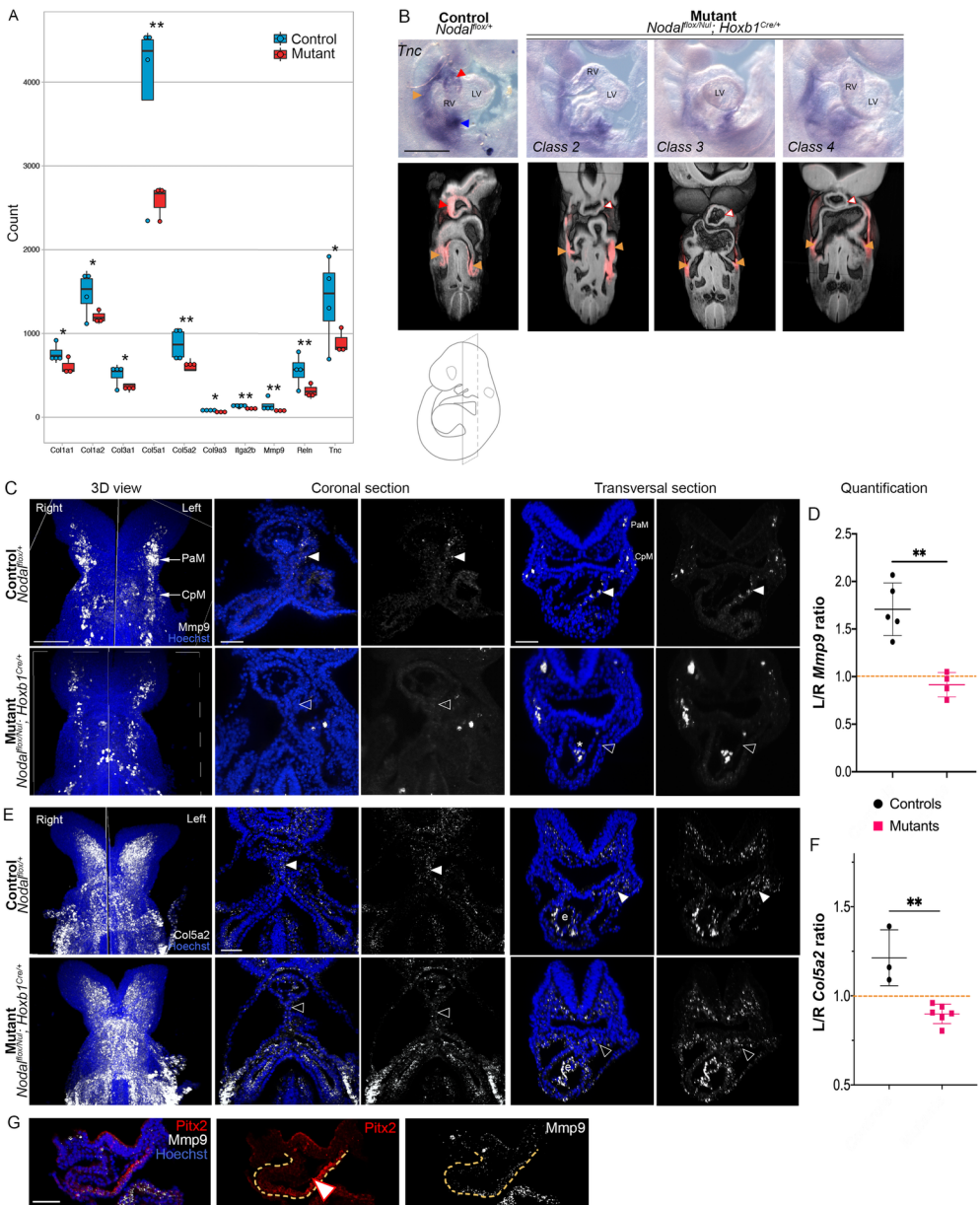


Figure 5









**Table 1 : Situs of visceral organs and congenital heart defects at perinatal stages (E18.5 and P0).**

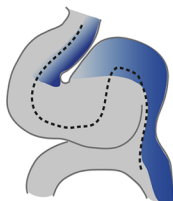
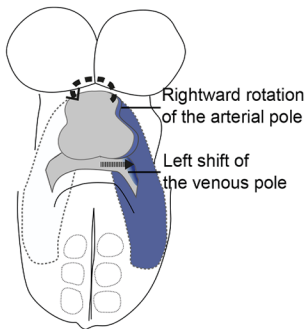
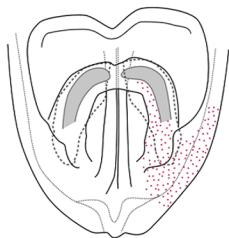
	<b>Control (n=10)</b> <i>Nodal<sup>flox/+</sup> ; Hoxb1<sup>+/+</sup></i>	<b>Mutant (n=33)</b> <i>Nodal<sup>flox/Nul</sup> ; Hoxb1<sup>Cre/+</sup></i>
<b>Heart apex position</b>		
Levocardia	100%	43%
Mesocardia	0%	21%
Dextrocardia	0%	36%
<b>Heart malformations</b>		
Complete atrioventricular septal defect	0%	100%
Malposition of the great arteries	0%	100%
Right atrial isomerism	0	70%
<b>Bronchi anatomy</b>		
Situs solitus	100%	0%
Right isomerism	0%	100%
<b>Colon flexure</b>		
Normal	100%	64%
Abnormal	0%	36%
<b>Spleen position</b>		
Situs solitus	100%	100%
<b>Liver lobation</b>		
Situs solitus	100%	100%
<b>Stomach position</b>		
Situs solitus	100%	100%

10/31 *Nodal<sup>flox/Nul</sup> ; Hoxb1<sup>Cre/+</sup>* mutants were recovered at E18.5 and 23/150 at P0, indicating normal Mendelian ratios (p=0.96, n=181, chi-square test). Right atrial isomerism is defined by the symmetry of the right atrial appendages. See Desgrange et al., 2019 for the phenotyping nomenclature.


Transient Nodal signalling in heart precursors E8.5c-d → Amplification and coordination of asymmetries at the tube poles E8.5f → Robust heart looping E9.5

Right

Left

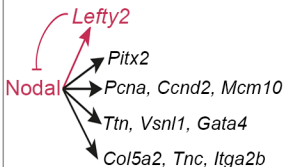


 Nodal signalling

 Heart precursors

 Cardiomyocytes

 *Nodal-ASE-LacZ*



Cell Proliferation

Cardiomyocyte differentiation

Extracellular matrix

Rightward helix  
of the  
heart tube